nuclear weapons journal

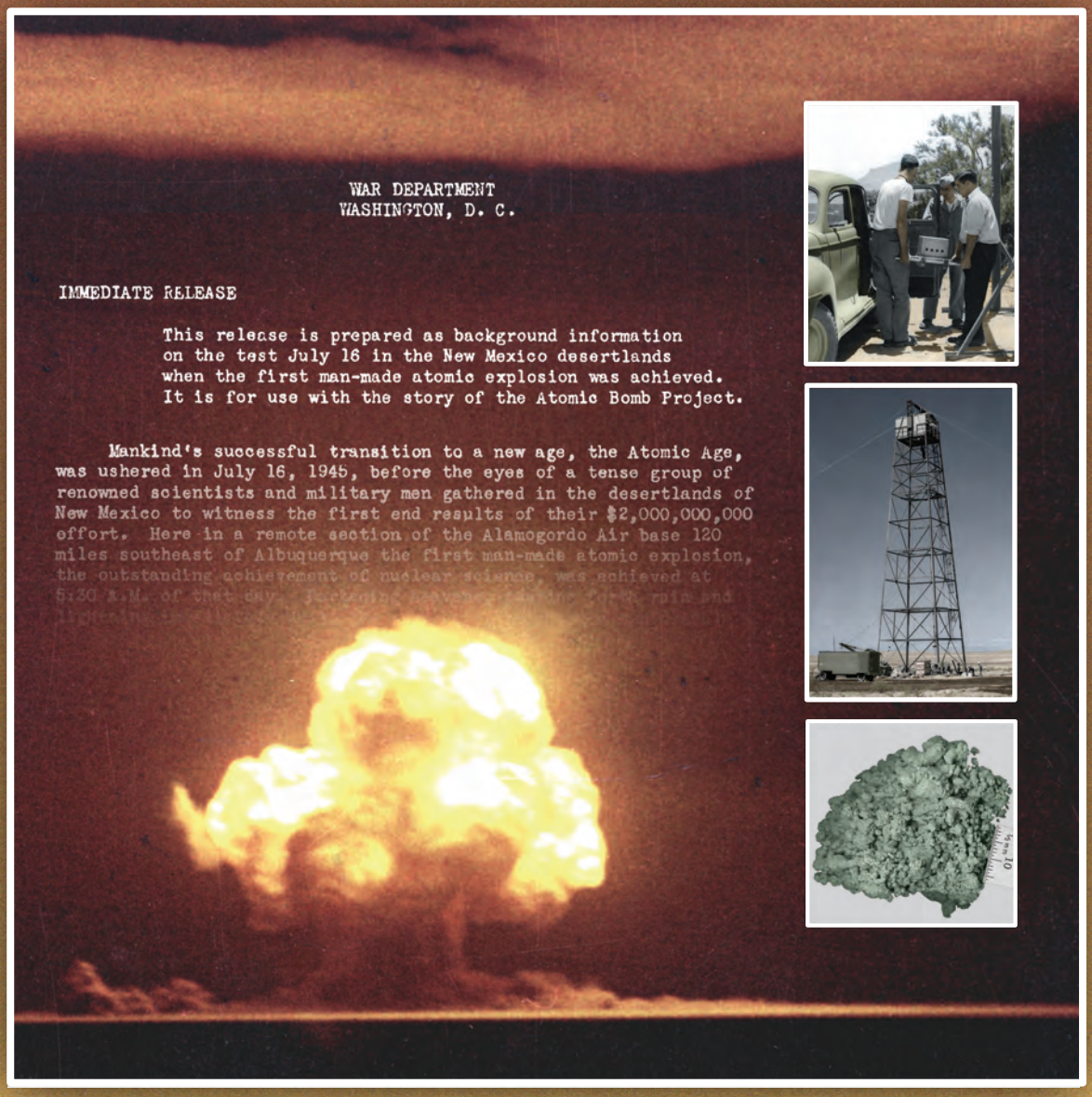

Issue 2 2005

Contents

About the cover: Sixty years after the first test of the atomic bomb at Trinity Site on White Sands Missile Range, scientists collected samples of trinitite—soil fused by the explosion—to back-calculate probable conditions of the 1945 blast. In A Backward Glance: Eyewitnesses to Trinity, witnesses describe what they saw from their locations near the site. Trinity's 60-year-old technology is markedly different from that of the current nuclear weapons work highlighted in this issue.

Issue 2, 2005 LALP-05-067

Nuclear Weapons Journal highlights ongoing work in the nuclear weapons program at Los Alamos National Laboratory. *NWJ* is an unclassified, quarterly publication funded by the Nuclear Weapons Program Directorate.

Managing Editor-Science Writer
Margaret Burgess

Science Writer-Editors
Larry McFarland
Jan Torline

Designer-Illustrator
Randy Summers

Editorial Advisor
Jonathan Ventura

Technical Advisor
Sieg Shalles

Printing Coordinator
Lupe Archuleta

Send inquiries, comments, and address changes to *nwpub@lanl.gov* or to
Los Alamos National Laboratory
Mail Stop F676
Los Alamos, NM 87545

Los Alamos NATIONAL LABORATORY EST. 1943

The World's Greatest Science Protecting America

NNSA National Nuclear Security Administration

Point of View

Preparing for the Future: Transforming the Stockpile

Edgar M. Vaughan, Lt. Col., USAF
Air Force Fellow
Los Alamos National Laboratory

For the past 10 years, NNSA's Stockpile Stewardship Program (SSP) has successfully maintained the nation's nuclear stockpile. SSP focused on four key elements:

- science-based understanding of the behaviors of warheads throughout their life cycles,
- careful surveillance of the stockpile,
- no new nuclear testing, and
- life extension programs (LEPs) for warhead refurbishment.

Unfortunately, the LEP approach may not be sustainable long-term. Over the next 40 years, LEP cost and manpower requirements will severely strain US resources. In fact, the projected costs to execute the SSP as planned exceed projected budgets.

Under the Administration's guidance (the Moscow Treaty), the United States and Russia will limit strategic nuclear forces to some 1,700 to 2,200 deployed weapons by 2012. A number of weapons will also be maintained as a reserve in the event of an unfavorable technical development with the deployed force. Maintaining this reserve force is becoming increasingly expensive in light of constrained budget resources. Compounding the budgetary constraints is the highly dynamic national security threat environment of the 21st century. In response to these pressures, NNSA is working to create a modern and responsive infrastructure.

Transforming the infrastructure, however, will require transforming the stockpile itself; our most credible option for this change is the reliable replacement warhead (RRW).

In the FY05 Consolidated Appropriations Act, Congress provided funds for an NNSA tri-lab initiative to determine the feasibility of designing, certifying, and manufacturing an RRW. In April 2005, the Nuclear Weapons Council established a Joint Project Officers Group (JPOG) to conduct a feasibility study for an RRW that is designed for use on submarine-launched ballistic missiles and that is compatible with intercontinental ballistic missiles. The FY06 Energy and Water Appropriations Act tripled the Administration's request for RRW from $9M to $25M.

> The successful RRW will demonstrate life-cycle cost savings while providing confidence in certification without nuclear testing.

LANL is teaming with Sandia National Laboratories/New Mexico and Lawrence Livermore National Laboratory is teaming with Sandia National Laboratories/California to design an RRW that will improve the safety, security, certifiability, and manufacturability of existing US warheads and their components.

Each team is charged with providing a preliminary design data package to the JPOG by March 31, 2006, and delivering a final report to the JPOG by August 31, 2006.

The final reports must include certification and manufacturing plans, a risk assessment,

continued on page 44

A New Look at Trinitite

Sixty years after the July 16, 1945, test of the first nuclear bomb (originally called an atomic bomb) at Trinity Site on White Sands Missile Range (WSMR) in New Mexico, we collected many samples of the soil fused by the explosion. This very slightly radioactive green glass is called trinitite.

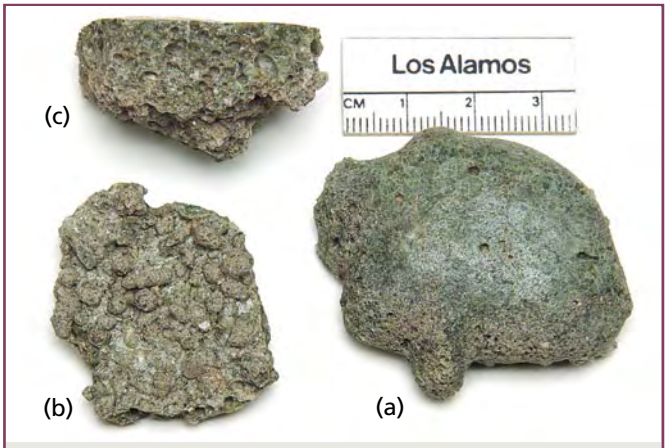

Three views of trinitite samples: (*a*), the top (blast side); (*b*), the bottom (ground side); (*c*), a side view showing the bubble voids (vesicles).

Our purposes were to use the properties of trinitite to calculate backward to the yield, fireball temperature, fireball duration, heat in the rising fireball, and the spread of ejecta from the Trinity test and to suggest that trinitite was deposited by a rain of molten droplets and puddling from the heat. Using our trinitite samples, we calculated some probable conditions of the nuclear explosion. We estimate the yield of the Trinity event was 9–18 kt, plus approximately 4.2 kt from the energy carried away by the mushroom cloud. We calculated an average fireball temperature of 8430 K, the duration of heating at approximately 3.1 s, and a crater depth of approximately 4 ft. These numbers compare reasonably well with the real-time measurements calculated 60 years ago and with unclassified published data.

If Trinity Site had not been cleaned up (bulldozed) by removing and/or burying a significant portion of the trinitite, a field survey would provide the numbers needed for our calculations. Because an explosion of plutonium formed the trinitite, most previous observations had a radiological emphasis. Our discussion is confined to macroscopic measurements and theoretical calculations of the blast based on a few assumptions. We show how observations of nonradiological trinitite properties and relatively straightforward calculations provide estimates of the event that produced the "lake of green glass" in 1945.

Yield Calculation

Most of our samples are approximately the size of a small pancake with similar thicknesses that include significant trapped bubble voids. The top (blast side) is smooth with a light green glassy luster. The bottom (ground side) is rough and light tan with sandy inclusions. Comparing our samples with an old photo, we conclude they are a reasonable representation of the glassy trinitite field. The average thickness of our samples is 1–2 cm; samples <1 cm or >2 cm in thickness are less common. Determining the thickness of the trinitite layer was critical in our yield calculation.

Another crucial number is the maximum radial extent R of the trinitite layer (thickness ΔL) from ground zero. We used aerial photos taken 28 h after the Trinity event to determine the radial extent. These photos show the trinitite layer extended to a radius of at least 300 m. We used a value of R = 300 m for the radial extent of the trinitite.

Undisturbed surface of the trinitite field.

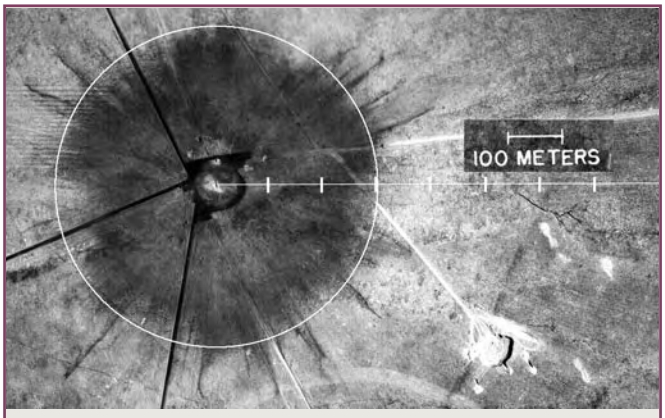

This aerial photo, taken 28 h after the Trinity test, shows that the trinitite layer extends to a radius of 300 m. The spikes indicate that the trinitite layer may extend as far as 400 m.

The initial burst of intense γ radiation probably vaporized much of the water in the soil; this vapor was then swept away by the expanding fireball and likely lost to posttest inventory. We cannot calculate this heat loss without using Trinity test measurements of γ-ray intensity, but we include a water vaporization estimate to show it is probably a small effect.

To estimate the yield, we imagine the explosive device was detonated in the air but was surrounded by a spherical shell of soil material of radius R and ask how much heat would be needed to melt or otherwise transform a layer of thickness ΔL of this material. We assert that this imagined spherical situation gives us information on the actual hemispherical configuration. The heat can be estimated from a formula for the heat per unit volume Q/V,

$$Q/V = q = (C\Delta T + h^T + h^R)\rho \,, \qquad (1)$$

with C the specific heat, ΔT the temperature rise, h^T and h^R the heats of transformation/reaction of material components, and ρ the density. Because we need a heat value for each component of the ground material, for simplicity we assume it was an arkose (mostly quartz) sand. The heat content Q of each component is $Q = qV$, and the total heat content is a sum of terms like this. We ignore the heat of reaction and assume the arkose sand is made entirely of quartz and free water. We need only the volume of a thin shell at a large radius, so

$$V = 4\pi R^2 \Delta L_c \,, \qquad (2)$$

if $\Delta L_c << R$ and ΔL_c is the equivalent thickness of the appropriate component.

The following constants for quartz and water were used to get q.

Constant	Units	Quartz	Water
C	cal/g °C	0.24	1.0
ΔT	°C (from 10°)	1660 mp uncertain	90 bp
h^T	cal/g	37 $\alpha \rightarrow \beta \rightarrow$ liquid	585 $\rightarrow$ vapor
ρ	g/cm³	1.8	1.0
q_c	cal/cm³	784	675

The average density of several trinitite pancakes is much lower than that of pure quartz {ρ = 2.7 g/cm³} because bubble voids account for approximately 33% of the total trinitite volume. If ΔL_c is the equivalent thickness of water per observed trinitite thickness ΔL, the total heat of soil plus water per volume of trinitite is

$$q = [q_c(\text{quartz}) + q_c(\text{water})\Delta L_c/\Delta L] \,. \qquad (3)$$

We get the following for the total heat per observed volume of trinitite.

$\Delta L_c/\Delta L$	q(cal/cm³)
0	784
0.02	798
0.1	852

We neglect bound water and other volatiles that may have been in the sand. Vaporization of water increases the q values by approximately the same percentage as water present in the sand and is small for the small amounts of water expected.

The volume V of the spherical shell (with R = 300 m) is calculated as

V(cm³) with R = 300 m assuming the following:

ΔL (cm)	V (10^{10} cm³)
1.0	1.13
1.5	1.7
2.0	2.26

If the above values for q (2% water) and V are used with the conversion factor, 1 kt TNT equivalent = 10^{12} calories, we get the following possible yields.

ΔL (cm)	Yield (kt)
1	9.0
1.5	13.5
2.0	18.0

These yields are well within published yield ranges and vary by an approximate factor of 2. The trinitite was not uniformly spread over the area: some was thicker than 2 cm, some was thinner than 1 cm, and in some places there was no trinitite. Nonetheless, we believe that these yields well represent the average disposition of energy. We also need to add considerable energy (estimate 4–5 kt) of processes whose properties are more difficult to extract from the trinitite layer (see Heat in the Rising Fireball, p. 6).

Fireball Temperature

In theory, the thermal conductivity of the ground material (sand) together with the heat diffusion equation should give us the temperature of the fireball. In practice, thermal conductivity and other constants vary wildly for different materials. Nonetheless, our temperature calculation compares favorably with the measured values published by the Atomic Energy Commission. In keeping with our previous yield calculation, we solve the heat diffusion equation with approximate methods; we begin with the definition of thermal conductivity H as usually used in its experimental determination. The heat flow Q through a slab of material of area A, thickness $\Delta\ell$, in a time Δt is

$$Q/A = H(T_b - 2T_m + T_c)\Delta t/\Delta\ell \,. \qquad (4)$$

Here T_b is the temperature of one face of the slab material, T_m is the middle temperature, and T_c is the temperature of the other face. We have also used a second order finite difference to approximate the spatial derivative on the right-hand side of Eq. (4).

We intend to relate $\Delta\ell$ to the thickness of the trinitite layer ΔL. The average temperature of the fireball is T_b and T_m is a temperature near the melting temperature of the material. The time the hot fireball was in contact with a slab or globule of material is Δt.

A variation of Eq. (1) gives the heat content of the slab

$$Q/A = C\rho(T_m - T_o)\Delta\ell \,, \qquad (5)$$

with T_o the initial temperature.

In addition, we assume the fireball (especially inside) radiates as a black body, so the heat flux is

$$Q/A = e\sigma(T_b^4 - T_m^4)\Delta t, \qquad (6)$$

with σ the Stefan-Boltzmann constant and e the emissivity.

Equations (4), (5), and (6) can be solved for three unknowns. We eliminate Q/A from pairs of equations, reduce the system to two equations, and then solve for T_b and Δt.

Define $\Gamma = H/\sigma$ and solve Eqs. (4) and (6) to get

$$T_b^4 - T_m^4 = (T_b - 2T_m + T_c)\Gamma/e\Delta\ell \,. \qquad (7)$$

Assume the slab is heated equally on all sides so $T_c = T_b$. Use the identity $(x^4 - y^4) = (x^3 + x^2y + xy^2 + y^3)(x - y)$, define $\theta = T_b/T_m$, divide by T_m^3, and simplify to get

$$\theta^3 + \theta^2 + \theta + 1 = 2\Gamma/e\Delta\ell T_m^3 \,. \qquad (8)$$

This equation expresses θ (or T_b) in terms of known quantities Γ, e,$\Delta\ell$, and T_m. The factor 2 comes from the numerical approximation for the derivative and is essential. It is basically a geometric shape factor. Admittedly, our "known" quantities are not well known, but if we use the following,

σ = 1.36 x 10^{-12} (cal/s cm^2 K^4),
H = 0.006, sandstone (cal/K s cm),
Γ = 2.3 x 10^{10} (K^3 cm),
e = 0.3, aluminum oxide (porcelain)—dimensionless,
T_m = 1943 K, and
$\Delta\ell$ = 0.2 cm,

we get $\theta = 4.34$. One can verify this by substitution into Eq. (8). This gives an average fireball temperature of $T_b = 8430$ K.

Note that we have used a globule thickness $\Delta\ell = 0.2$ cm instead of the value of approximately 1.5 cm we used for the yield calculation. That is, the trinitite layer on the ground is approximately seven times the value used in the temperature calculation. We do this for two reasons.

- Theory—If a larger value for $\Delta\ell$ is used, the fireball temperature comes out much too small and, more important, the time for heating (see Eq. [10]) is much too long.

- Observations—Many small (2-mm-diameter) spheroids of trinitite were recently collected from the Trinity Site. Their diameters correspond well with the $\Delta\ell = 0.2$ used in the temperature/time calculation. It seems reasonable that these objects were formed in the air and not formed on the ground. In fact, we also found semi-glassy agglomerations of small-diameter spheroids together with other ejecta shapes.

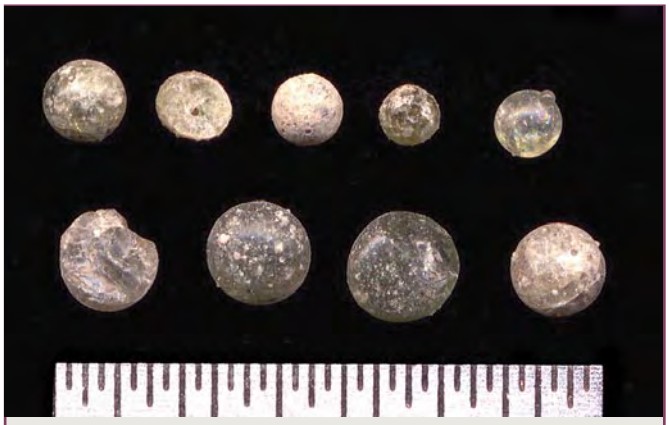

Trinitite spheroids of 2-mm-diameter recently collected from Trinity Site.

We might conclude that much of the layer was formed not on the ground but by a rain of material injected into the fireball that melted, fell back, and collected on the hot sand to form the observed puddles of trinitite, especially within the radius of the hottest part of the event. After falling on the ground, the top surface of the trinitite layer was still heated somewhat by the fireball and thus developed a smooth surface. The bottom surface, being

Agglomeration of 2-mm-diameter trinitite spheroids, which contains radioactive hot spots.

cooler and protected by the continual rain, retained a record of the first beads deposited.

Fireball Duration

We can also estimate the time needed to melt a 0.2-cm globule. Define $\kappa = H/C\rho$, solve Eqs. (4) and (5), again with $T_c = T_b$, to obtain

$$(T_m - T_o)/\Delta t = 2\kappa(T_b - T_m)/(\Delta\ell)^2 \,, \qquad (9)$$

which is the heat diffusion differential equation in disguise. The factor κ is the heat diffusivity. Instead of κ, here we prefer to use $\mu = 1/\kappa = C\rho/H$. Assuming $T_o/T_m << 1$, solve Eq. (9) for Δt to obtain

$$2\Delta t = \mu\,(\Delta\ell)^2/(\theta - 1) \,. \qquad (10)$$

Note how this formula is intimately coupled with the previously calculated fireball temperature θ.

If we use the following numbers,

κ = 0.011, diffusivity of sandstone,
ρ_s = 2.4, density of sandstone, included in κ,
$\mu/2$ = 45.5 s/cm², and
θ = 4.34, our previous calculation (a dimensionless temperature),

we obtain

$$\Delta t = 13.6(\Delta\ell)^2 \,.$$

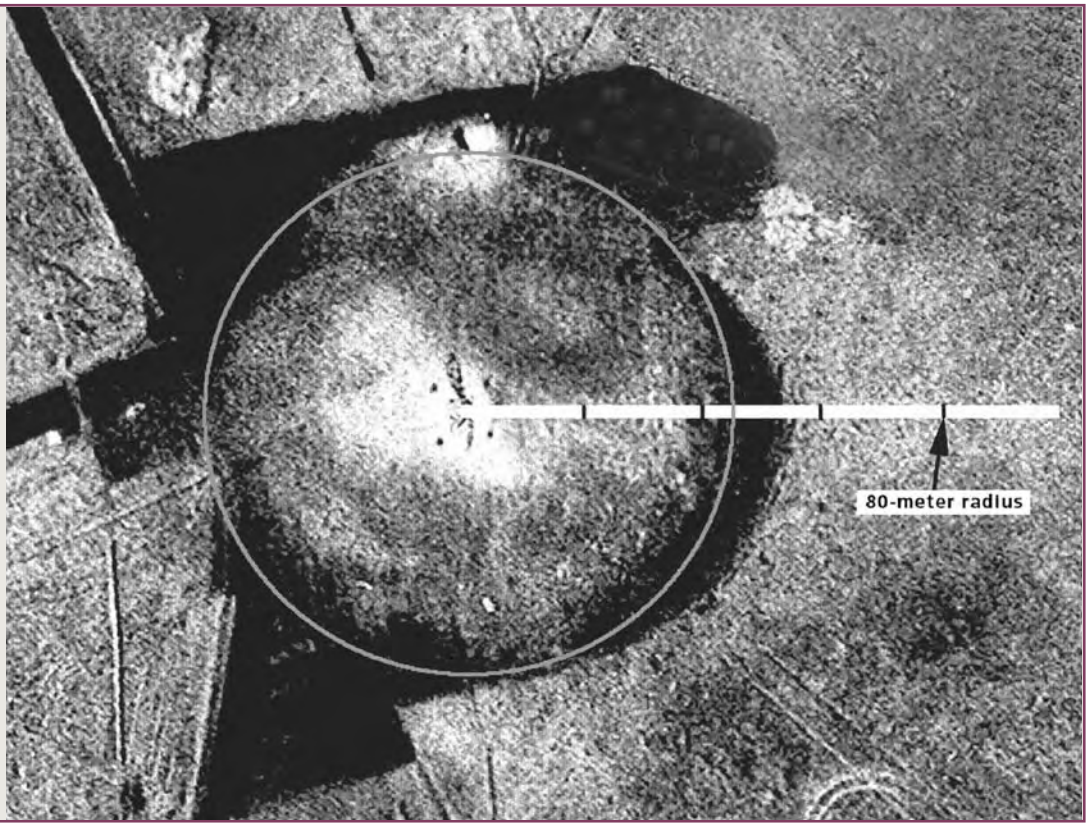

Aerial photo taken 28 h after the Trinity test. Photo shows the location of the four tower posts that held the nuclear device and the 55-m radius of pretest blacktop. A 40-m inner radius of the blacktop shows removed material after the test; 40 m is the assumed radius of the crater formed by the explosion.

Because many of the trinitite beads are solid, we used a density of 2.4 for sandstone instead of 1.8 that was used for the bubbly trinitite layer. The time for melting a globule with $\Delta\ell = 0.2$ cm is $\Delta t = 0.55$ s.

To make Eq. (4) consistent with the yield calculation, we need to multiply Δt and $\Delta\ell$ by a common factor, for example N, so $\Delta\ell$ will agree with the observed thickness; thus (with $\Delta L = 1.5$)

$$N = (\rho\,\Delta L)/(\rho_s\,\Delta\ell) = [(1.8)\,(1.5)]/[(2.4)\,(0.2)] = 5.6\ ,$$

and the total time for the Trinity event was $N\Delta t = 3.1$ s. The density ratio ρ/ρ_s is needed to account for the expanded thickness of the trinitite layer caused by the bubbles. This calculated time corresponds well with the approximations of an on-site observer of 3–4 s for the neck or stem to form after the fireball started to rise from the ground.

Equation (10) shows how a larger globule size $\Delta\ell$ increases the time to much larger (and unacceptable) values. For comparison, the trinitite "rain" rate was $\Delta\ell/\Delta t = 0.36$ cm/s = 500 in./h; rain from an intense thunderstorm or hurricane occurs at a rate of approximately 10 in./h.

Heat in the Rising Fireball

Much of the energy from the Trinity explosion escaped in the hemisphere of heated air that rose from the ground after approximately 3 s. We can estimate this escaped heat with a variation of Eq. (5)

$$Q_a = C_a(T_b - T_o)\rho_b V_a\ , \qquad (11)$$

where C_a is now the heat capacity of air and V_a its hemispherical volume with a temperature T_b. The volume V_a is

$$V_a = (1/2)(4/3)\pi R^3 = 2.09R^3\ . \qquad (12)$$

Estimate R with the approximate radius previously used for the extent of the trinitite layer. Estimate T_b with the average calculated fireball temperature. The fireball density ρ_b is much lower than that of the ambient air because it has been heated to a very high temperature and much air has been expelled by the shock wave. If we assume the fireball ceased to expand because its pressure equalized with the ambient atmospheric pressure, we can use the ideal gas equation of state to estimate the density ρ_b:

$$\rho_b T_b = \rho_o T_o \text{ , or } \rho_b = \rho_o (T_o/T_b) \text{ ,} \qquad (13)$$

where ρ_o and T_o are the ambient density and temperature, respectively. Substitute Eqs. (13) and (12) into Eq. (11) to get Q_a:

$$Q_a = 2.08 R^3 C_a \rho_o T (1 - T_o/T_b) \text{ .} \qquad (14)$$

Because $T_o << T_b$, most of the variation comes from the R^3 term. If the following values are used,

C_a = 0.26 cal/g °C,
ρ_o = 1.04 x 10^{-3} g/cm³ (the density of air at the 5000-ft altitude of Trinity Site),
T_o = 283 K, and
T_b = 8430 K,

we find

$$Q_a(R = 300 \text{ m}) = 4.2 \text{ kt .}$$

This value must be added to our yield calculation because the rising fireball might have carried away approximately 31% of the explosion's energy. This percentage compares favorably with more precise and complicated calculations.

Spread of Ejecta

More support for our contention that much of the trinitite layer was laid down by a "rain" of molten droplets can be found by looking at the amount of material ejected by the blast in forming the crater at ground zero. Considerable confusion exists in the nontechnical and historical literature regarding the dimensions of this crater because

- the crater diameter was confused with the radius of the trinitite layer (~300 m) and
- the ground (porous sand) underwent considerable plastic compression by the force of the blast wave.

Hence the actual depth of the crater is usually overestimated.

A photo taken after the Trinity test shows a 40-m-radius area of removed material that we take to be the crater. If we assume the trinitite layer came from this crater, we can back-calculate the crater depth from the spread and thickness of the trinitite layer with the following calculation.

Assume R_c and Δd are the radius and depth of the crater. Assume a parabolic or spherical profile (with $\Delta d << R_c$) for the crater and its mass as $M_c = \pi \rho_s R_c^2 \Delta d/2$. Assume an annular cylindrical shape for the trinitite layer of outer radius R, inner radius of R_c, and thickness ΔL; its mass will be $M_t = \pi \rho (R^2 - R_c^2) \Delta L$. Let $\alpha = R/R_c$, $\beta = \rho/\rho_s$, equate M_t and M_c, and solve for Δd to get

$\Delta d = 2 (\alpha^2 - 1) \beta \Delta L$ (15) for the crater depth.

The number 2 is a geometrical factor that depends upon the ratio of the shape profiles of the two volumes and has a range of approximately 1 to 2. If we use the values

R = 300 m, R_c = 40 m : α = 7.5,
ρ = 1.8 g/cm³, ρ_s = 2.4 g/cm³ : β = 0.75,
ΔL = 1.5 cm,

we get

Δd = 124 cm, a crater depth of roughly 4 ft.

This approximation is very near the measured depth of 4.7 ft. Our values for the trinitite layer give a volume of 3,100 m³ with a mass of approximately 7,500 metric tons. It is tempting to attribute the additional 0.7 ft of the measured depth to material that was vaporized or swept away by the mushroom cloud (fallout outside the main area of the trinitite), by as much as 15% of the total volume, but our calculations may be too crude to reach this conclusion. NWJ

Point of contact:
Robert E. Hermes, 667-0276, rhermes@lanl.gov

Coauthor William B. Strickfaden is a physicist who retired from P. E. Systems of San Diego, California. He also was a student at Los Alamos Scientific Laboratory. Other contributors to the research include Jim Eckles and his team from the WSMR and Roger Meade of LANL.

Neutron Tube Target Loading

Neutron generators are used in all weapon systems in the US nuclear weapons stockpile. These limited-life components supply a burst of neutrons that ensures initiation of the fission chain reaction in a nuclear weapon. The generators operate by creating and accelerating a beam of deuterium atoms (ions) into a solid target that contains

The NTTL team has consistently achieved high production yields.

tritium. The fusion reaction of the deuterium and tritium atoms produces the neutrons required to initiate fission. Tritium decays over time; therefore, neutron generators are replaced periodically as part of the stockpile stewardship mission. The process of loading tritium into targets is called neutron tube target loading (NTTL).

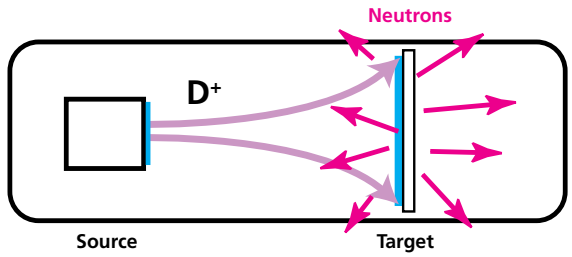

How does a neutron tube generate neutrons? A neutron tube accelerates deuterium ions (D^+) onto a tritium-loaded target. The resulting deuterium-tritium fusion reaction produces the required neutrons.

Neutron generators were produced at the Pinellas Plant in Florida until 1996. As part of the Nonnuclear Reconfiguration Program, DOE closed Pinellas and transferred the neutron generator production mission to Sandia National Laboratories New Mexico(SNL/NM). At that time, SNL lacked both tritium processing experience and the requisite nuclear infrastructure to support tritium operations. On the other hand, LANL had both the expertise for tritium research and development (R&D) and a robust nuclear facility infrastructure.

To take advantage of LANL's extensive tritium experience, DOE assigned the NTTL mission to Los Alamos.

After the mission transfer, LANL reengineered the Pinellas NTTL process and designed, fabricated, and installed hardware. LANL's comprehensive parametric study of the loading process resulted in optimal process parameters. The first War Reserve (WR) targets produced at LANL were shipped to SNL in March 1998. During the more than

Neutron generator (*right*) and neutron tube (*left*), with 1.25-in.-diameter target (*inset*). All nuclear weapons systems in the US stockpile contain neutron generators that supply a burst of neutrons to ensure initiation of the fission reaction. The units contain tritium and because tritium decays over time, the neutron generators must be replaced periodically.

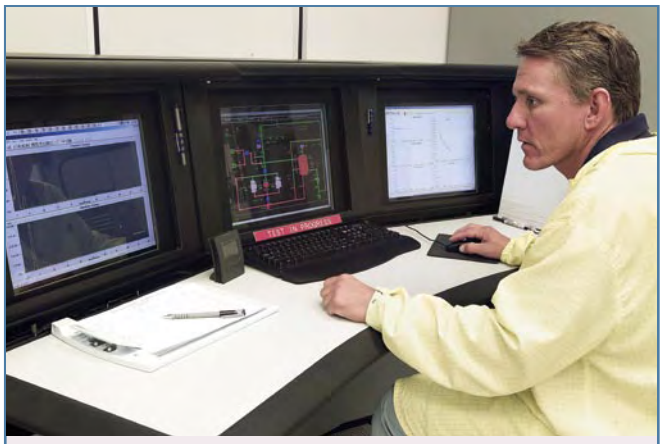

Managing the tritium loading process through the data acquisition and control station interface.

7 years since achieving WR process qualification, the NTTL team has successfully loaded, packaged, and shipped more than 4,500 WR targets. To maintain DOE standards for WR qualification, LANL's NTTL process continues to meet strict weapons quality criteria.

The Tritium Science Engineering Group is responsible for receiving unloaded neutron tube targets from SNL, loading the targets with tritium, and shipping the loaded targets to SNL for assembly into neutron tubes and, ultimately, into neutron generators.

All shipments of loaded WR targets have been on or ahead of schedule, and more than 95% of the targets have successfully passed the loading verification process at SNL. The NTTL team has also successfully loaded, packaged, and shipped more than 1,600 development, shelf-life, and field-test targets, controlatrons (for testing neutron tubes), and neutron-scattering films.

The NTTL team has consistently achieved high production yields (significantly higher than those of Pinellas), maintained production schedules, and delivered a high-quality WR product. The NTTL team also continued to make process improvements since 1998, including

- an improved integrated target shipping/storage system,
- custom-designed tools and fixtures for target manipulation,
- an advanced heater for the loader vacuum chamber that reduces processing time,
- a near-real-time energy-dispersive analysis capability for process monitoring,
- an improved software-based data acquisition and control system,
- an improved configuration of thermometry for ease of measurement and test equipment replacement, and
- an improved Department of Transportation-compliant packaging/shipping configuration.

The LANL NTTL process is also safer than the former Pinellas process because it takes place in an inert glovebox instead of a fume hood and required tritium inventory is significantly less. The LANL process generates less radioactive waste, which results in significantly less operator exposure and environmental impact.

Currently, NTTL production takes place at LANL's Technical Area 21 Tritium Science and Fabrication Facility. One loader is operational with tritium for WR production work. A second loader, the loader test stand (LTS), is operational with deuterium. The LTS is used for process development, training, and troubleshooting and as a test platform. Three

Manipulating an incoming WR target in preparation for the tritium loading process.

Inspecting loaded target inventory held under vacuum prior to target packaging, stamping, and shipping.

loaders, not including the LTS, were eventually to be made operational to meet production capacity requirements, approaching 3,500 targets per year.

In June 2005, NNSA decided to transfer the NTTL mission to SNL in Albuquerque. The two drivers for this decision were consolidating all neutron generator production activities and reducing operating costs. By including the transfer of all the LANL-designed loader hardware to SNL, NNSA has assured mission transfer success. Furthermore, LANL NTTL staff has been asked to share its expertise in thin-film hydriding and tritium handling with SNL to help the NTTL mission transfer succeed. Until the NTTL production capability is reestablished at SNL, LANL will retain the responsibility for loading targets and is expected to load approximately 1,000 targets for the W76 and W80 neutron generator programs.

LANL's reengineering of the NTTL process and the reestablishment of WR tritium loading of neutron tube targets are examples of the successful application of R&D capabilities and operations expertise to a production mission. Bringing together expertise, engineering, and dedication to science-based manufacturing culminated in the NTTL success story at LANL. NWJ

Point of contact:
Warren Yamada, 667-8614, yamada@lanl.gov

Contributors to the NTTL mission are Elizabeth Francois, Wallace Harbin II, Richard Hawes, Benjamin Roybal, Fred Steinkruger, and Thomas Venhaus, all of the Tritium Science Engineering Group.

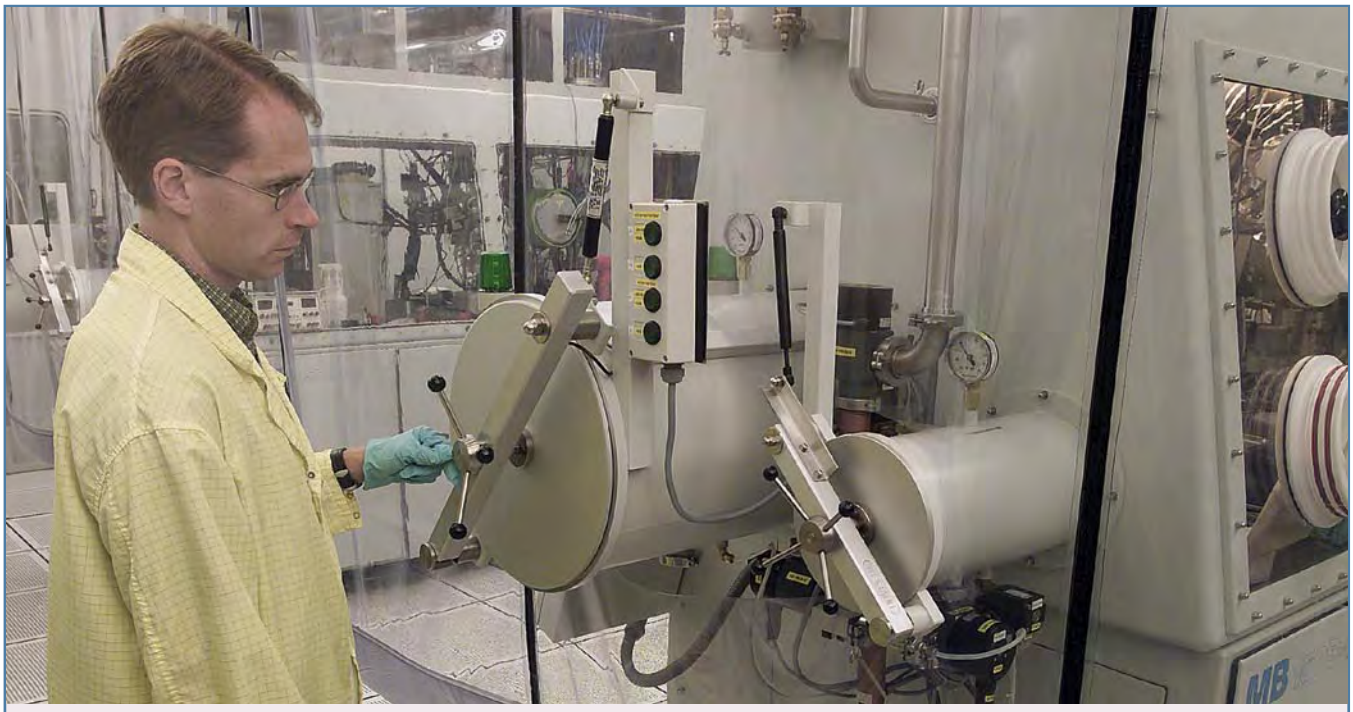

Activating the evacuation/purge cycle prior to glovebox pass box operations. (A pass box provides a way to safely insert material into a glovebox or remove material from it.)

Producing Nanoporous Metallic Foams

Producing nanoporous metals has been a difficult and, depending on the type of metal, elusive task. Recent discoveries by our team of researchers in the LANL Materials Dynamics Group have led to a method for achieving the combustion synthesis of nanoporous transition-metal foams that have ultralow densities and ultrahigh surface areas. (See "What are transition metals?" on page 15.) We have produced nanostructured metal foams of iron, cobalt, silver, and copper, and our nanofoam forming technique can be applied to many other metals. These materials offer a wide variety of potential applications in, for example, catalysis, fuel cells, and hydrogen storage.

Nanofoam pore diameters are measured in nanometers, too small for the unaided human eye to distinguish. In fact, the finest flaxen human hair, at diameters of 17 to 50 µm, is close to the limit of resolution of the human eye. The smallest pores in our metal nanofoams are 10 to 20 nm in diameter, about a thousand times smaller. The largest pores, at 1 to 3 µm, are still too small to see.

To produce a nanostructured metal foam, we ignite pressed pellets of high-nitrogen metal complexes in an inert atmosphere at different pressures. As a pellet rapidly burns, its volume dramatically increases; the burning complex releases heated metal atoms, which attract each other and coalesce into larger particles. At the same time, decomposition gases such as hydrogen and nitrogen, also released by the reaction, blow tiny holes through the coalescing metal to form nanoscopic pores. The resulting foams typically contain 50% to 70% metal, with the remainder being carbon nitride-type impurities that can be removed later by heat treatment.

Possible applications for our nanostructured metal foams abound, including catalysis, fuel cells, and hydrogen storage.

The iron foam has the incredibly low density of 0.01 to 0.04 g/cm^3. For comparison, ultralow-density aluminum foam has a density of 0.08 to 0.16 g/cm^3.

Our nanofoams have pore diameters of 10 to 20 nm to about 1 µm, surface area-to-mass ratios as high as 258 m^2/g, and densities as low as 0.01 g/cm^3. For comparison, silica aerogels, the lightest known

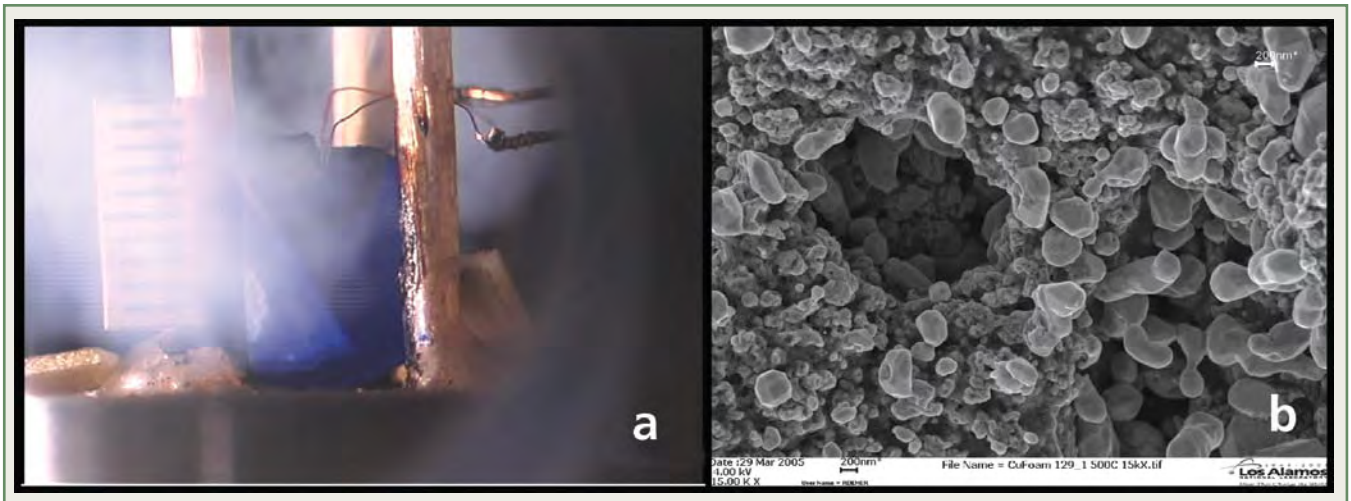

Copper nanoporous material formed at 200 psi Ar (the production vessel is pressurized with argon) overpressure: (*a*) burn front is dark portion heading top to bottom and (*b*) heat treated to 500°C in hydrogen gas (15,000x, 200-nm scale bar). Illustration (*a*) shows the actual formation of copper foam from the copper complex; (*b*) scanning electron micrograph (SEM) of copper heat treated to form copper foam.

solids, have mean pore diameters of approximately 20 nm, surface-to-mass ratios of 600 to 1,000 m^2/g, and densities of 0.003 to 0.35 g/cm^3, with the most common density being approximately 0.1 g/cm^3.

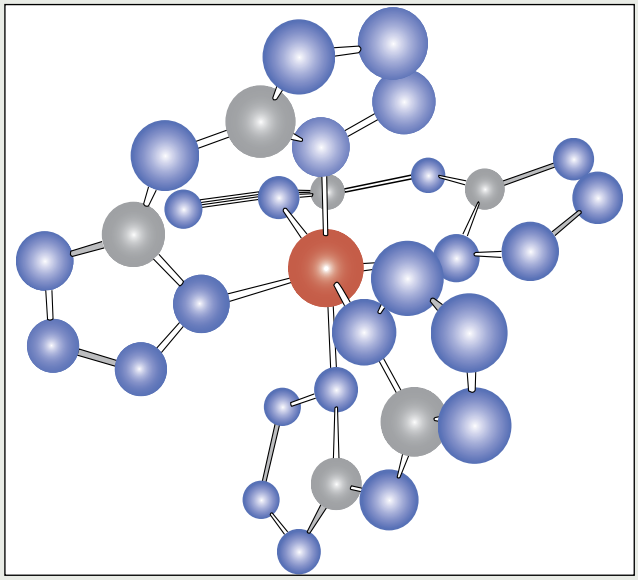

The $(NH_4)_3[Fe^{III}(BTA)_3]$ anion of iron-bistetrazolamine (Fe-BTA). This anion is the high-nitrogen transition-metal complex we use to produce iron nanofoam. This was the first material we investigated to produce metal foams. The blue spheres are nitrogen atoms, the gray spheres are carbon atoms, and the red sphere is an iron atom. We replace the iron atom with an atom of a different metal to produce a complex of a different metal. Not shown are the three ammonium cations surrounding the anion.

We have observed that heat-treating the iron foam can increase the surface area dramatically, in one case from 20 to 120 m^2/g. The surface area also seems to be dependent on the pressure of the inert gas during combustion, with a lower surface area and higher density obtained at higher overpressures. We also observe this trend in the small-angle neutron scattering (SANS) measurements of the as-formed iron material, which show that the average particle radius increases with increasing overpressure.

Key to this forming technique is the fact that these high-nitrogen transition-metal complexes burn rapidly but steadily. In our case, burning means a self-sustained exothermic reaction that occurs in the absence of oxygen. Most energetic metal complexes or compounds detonate rather than burn steadily, especially if they are made with transition metals. The steady burning of our special compounds allows the coalescing metal to largely stick together as the nitrogen blows through it, which is essential for pore formation. Steady burning also allows the nanofoam to form as a self-supporting "monolith"

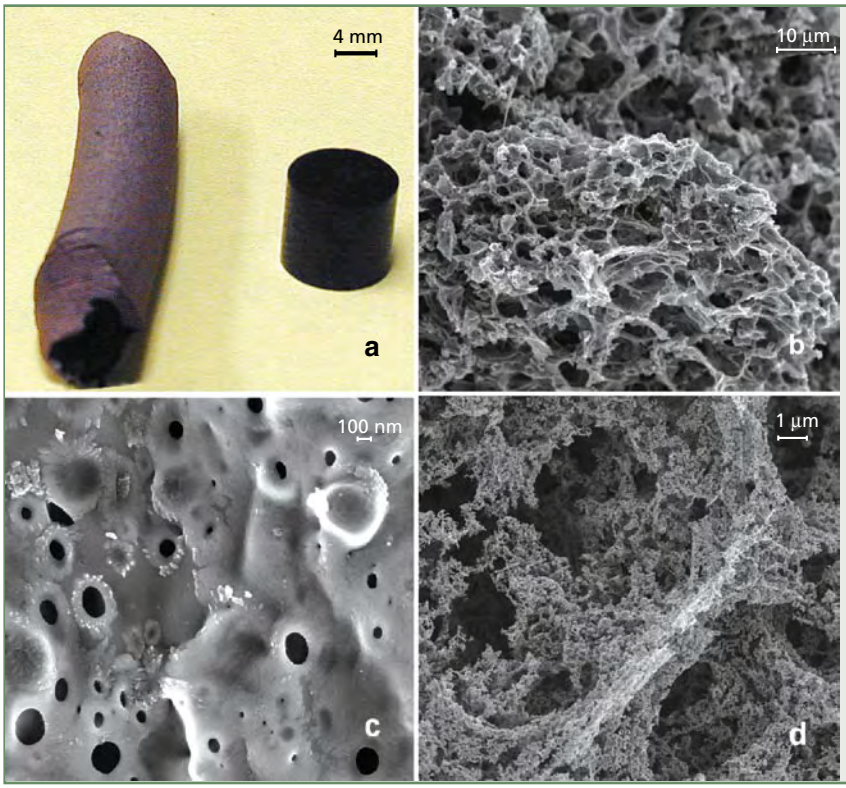

Iron pellet and examples of iron nanofoam: (*a*) photograph, 4-mm scale bar, of iron foam monolith next to unburned pellet of the Fe-BTA complex; (*b*) SEM, 10-µm scale bar, of low-pressure iron foam showing pore structure of roughly 1 µm; (*c*) SEM, 100-nm scale bar, of high-pressure iron foam showing pore substructure of roughly 20 to 100 nm; (*d*) SEM, 1-µm scale bar, of heat-treated iron foam.

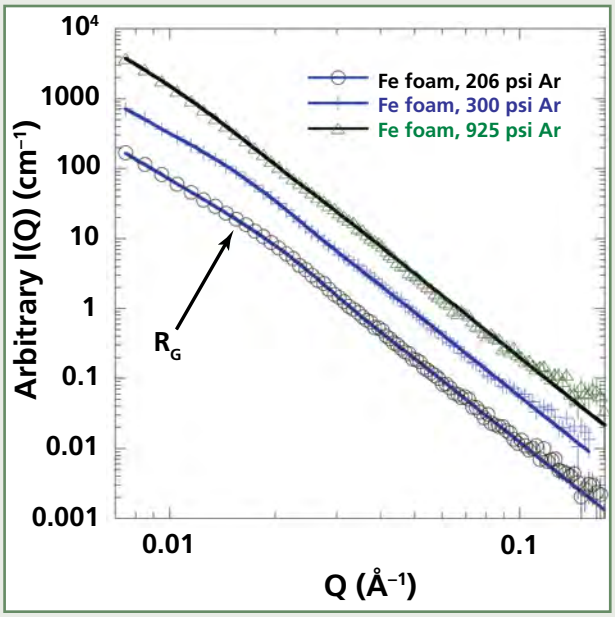

Log-log plot of SANS instrument scattering sector Q plotted against scattering intensity I(Q) per centimeter. The graph shows SANS measurement results for three iron foams formed at different pressures of 206, 300, and 925 psi Ar; the average radius of the particles in the foams is 146 ± 1, 182 ± 1, and 232 ± 6 Å, respectively. The Guimier region R_G, which indicates the average size of the scattering particles, shifts to lower Q values with increasing pressure, suggesting an increase in average particle size.

(one solid piece) rather than as a powder or a collection of exploded fragments. Self-support is important for the many catalytic applications for which our nanofoams can be used.

Several standard techniques are employed to prepare nanostructured metal monoliths. These techniques include the use of templates (such as polymers or aerogels), electrodeposition, and etching of noble metal alloys. Typically, the resultant nanoporous metals are available only as powders and thin films. Almost all these methods require template removal to access the nanoporous metals themselves. Thus the template removal process is a major obstacle to the preparation of nanoporous metallic materials.

The formation of monolithic structures that do not require templates in their production continues to be a formidable challenge. The ability to control, without the use of templates, the shape of the nanoporous metal as it forms would provide enormous benefits in applications such as catalysts, electrodes, and sensors. A second major challenge involves the ability to control the nature of the cellular structure. Understanding the factors that control pore size in these materials would be highly beneficial in terms of the design of nanoporous metals. A third challenge is the lack of generality and flexibility of the current methods for preparing nanoporous materials with a variety of different metals. The ability to prepare many different nanoporous metals would significantly expand the range and utility of the currently available materials.

Possible applications for nanoporous metals are numerous. One primary application surely will be in catalysis: a good catalyst achieves high reaction rates by providing (1) a large surface area for the reactant molecules to adsorb onto and (2) open pores so the reactants and products can freely flow to and from the surface. With large surface areas and (generally) open pores, nanostructured metal foams could have huge impacts on a wide variety of catalytic processes. Nanoporous metals typically exhibit very large surface areas and demonstrate the ability to store high volumes of material, properties that are particularly important in their use as catalysts. Nanoporous metals have found possible applications as high-surface-area catalysts on the surface of fuel-cell electrodes as well as catalysts for nitrogen oxide (NO_x) pollutant-removal applications. The market for all catalysts in the year 2000 approached $27 billion in the US alone. With the ever-increasing need to reduce and remediate environmental pollution, the need for new "clean" catalysts will continue to grow.

Fuel cells that produce electricity directly from methane or other higher hydrocarbons require active catalysts. However, properly fabricating the fuel cells' electrodes is crucial. A highly successful approach uses fuel-cell anodes made of copper—to provide high electrical conductivity and a high resistance to carbon poisoning (the deposition of carbon impurities), a common but undesired reaction with this type of fuel cell—and a metal oxide that is a good catalyst and ion conductor for the electricity-producing reaction. By dispersing oxide nanoparticles in our self-supporting copper nanofoam, we can combine copper's high electrical conductivity and the metal-oxide nanoparticles' high surface area in

a comparatively robust "cermet"(ceramic + metal) anode. Fortuitously, similar cermet catalyst systems have shown promise in NO_x removal.

Research is also under way to investigate the applicability of nanostructured copper and silver foams for the detection of explosives and other harmful agents using surface-enhanced Raman scattering (SERS). Raman spectroscopy can provide information about single molecules by detecting the light scattered inelastically from the molecules. The rather weak Raman effect is strengthened greatly when the molecules are attached to a metal substrate with roughness on the order of nanometers. It has been shown that extremely small quantities of various materials can be detected using SERS that employs nanostructured metal substrates. For example, SERS has been used to detect some environmental biological pollutants at levels as low as 0.1 ng.

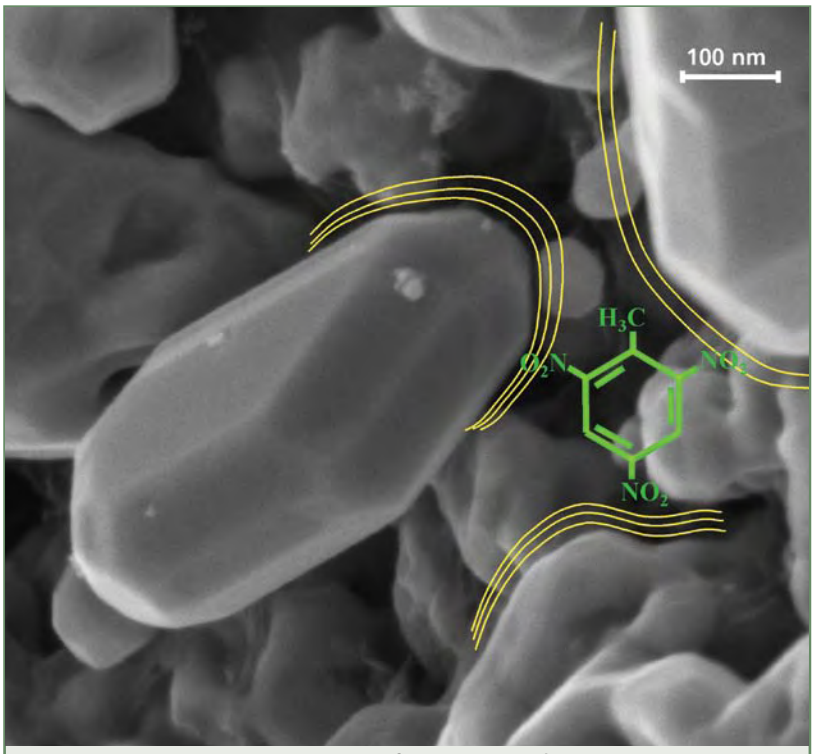

Schematic showing localization of illicit agent (green TNT molecule not to scale) into interstitial sites of metal foams for largest enhancements of Raman signal. The green hexagon is part of the TNT molecule. The yellow lines depict electronic effects occurring when a specific wavelength of light interacts with the metal, in turn leading to Raman signal enhancement when these electronic effects interact with the bound TNT. Cumulative electrostatic enhancements (yellow lines) from many surfaces could result when illicit substances (green TNT) bind into these sites.

SERS relies on electromagnetic interactions between the molecule to be detected and the substrate to which the molecule is attached. Because of the nanostructured foams' low densities, high surface areas, and stochastic structure, they appear to be ideal for SERS substrates. Materials of interest for SERS detection include chemicals as simple as glucose or as complex as anthrax as well as explosives.

The National Ignition Facility at Lawrence Livermore National Laboratory trains many intense pulsed laser beams on inertial confinement fusion (ICF) targets about the size of BBs. The targets contain fusion fuel—a frozen mixture of deuterium and tritium, two hydrogen isotopes. The laser beams heat and compress the fuel to the temperatures and densities required for fusion reactions to occur. Currently, an ICF target consists of a gold foam shell surrounding a nonporous shell filled with fusion fuel. To ensure that the shock waves generated at the target's surface travel efficiently into its interior, a shell of high-z nanostructured metal foam, such as copper, should surround the target. However, fabricating copper foam shells with the desired qualities has so far been difficult. We hope that this process for producing nanostructured metal foams will yield the pore sizes and densities that are useful in ICF applications.

Our metal nanofoam forming technique shows promise as a flexible, general approach to the formation of a wide range of new nanoporous metals not currently accessible by state-of-the-art nanoscience. Possible applications abound, not only in catalysis, fuel cells, and ICF, but also in applications ranging from hydrogen storage to electron field emission. Because the pore sizes, densities, and surface areas

are dramatically different from those of other metal foams currently being produced, there are sure to be many other interesting discoveries as more applications are investigated. NWJ

Point of contact:
Bryce Tappan, 667-0533, btappan@lanl.gov

Other LANL team members who contributed to this research include David Chavez, Darren Naud, Erik Luther, Michael Hiskey, My Hang Huynh, David Oschwald, and Steven Son.

This research recently won an *R&D Magazine* 2005 R&D 100 Award. This award program, which each year recognizes the world's top 100 scientific and technological advances, is designed to honor significant commercial promise in products, materials, or processes developed by the international research and development community.

What are transition metals?

The elements in the periodic table are often divided into four categories: main group elements, transition metals, lanthanides, and actinides. The main group elements include the active metals in the two columns on the extreme left of the table and the metals, semimetals (metalloids), and nonmetals in the six columns on the far right.

The transition metals, or transition elements, are the metallic elements in the columns in the center of the table, forming a bridge or transition between the active metals on the left and the elements on the right.

Lanthanides and actinides are usually shown in two rows below the main table; they are sometimes called the inner transition metals because their atomic numbers fall between the first and second elements in the last two rows of the transition metals (after lanthanum and actinium, respectively).

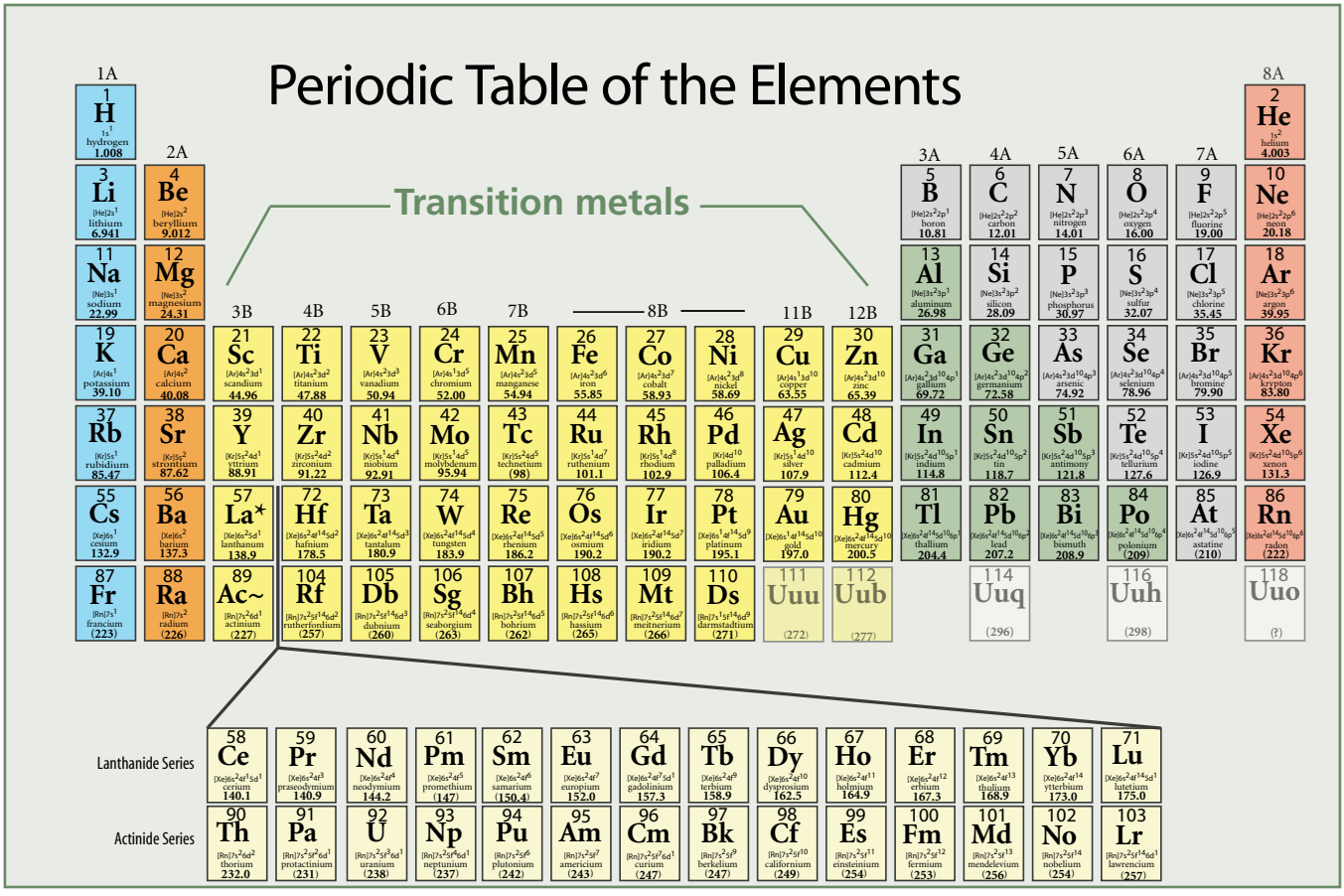

Joint Characterization, Analysis, and High Explosives Testing Conducted at the TA-16-340 Complex

In support of stockpile stewardship, the Materials and Explosives Engineering (MEE) Group of LANL's Engineering Sciences and Applications (ESA) Division has made significant progress modernizing and consolidating its high explosives (HE) manufacturing infrastructure.

To produce a lean, responsive, and cost-efficient HE processing facility, multiple operations are being consolidated at Technical Area 16 (TA-16), building 260, which is composed of 25 bays. Various operations can be conducted simultaneously in this explosives processing facility that is a hardened structure. One face of the building is composed of blowout walls that would rapidly vent pressure in the unlikely event of an accidental explosion. When an explosive is detonated, gas expands rapidly at high temperatures, causing high overpressures (shock waves) to form. These overpressures can result in injuries to personnel and damage to structures.

Building 260 after the 1959 machining accident.

Unfortunately, in 1959 two fatalities occurred at building 260. Approximately 7 lb of the HE PBX 9404 detonated during a manned HE operation when technicians drilled a 1/16th-in.-diameter hole into the HE. Since that time, Los Alamos engineers conducted small-scale tests and analyses that led to the development and implementation of operational safety procedures and devices. These include conducting only remote operations on sensitive explosives, employing blast doors that reflect and reduce the initial overpressures from the processing bays to the building corridors, and shutting down operations in adjoining and abutting pairs of bays based on the quantity of HE processed. However, none of these experiments examined the wraparound effects in which overpressures wrap around the end of a bay wall to dynamically affect the abutting bays. Wraparound effects were evident in the 1959 accident. In addition, concerns still exist with respect to the reflected shock waves from the blowout walls and overpressures experienced in adjacent bays, halls, and the corridors where remote operations are controlled and personnel work on other operations.

After HE is detonated, overpressures wrap around at the end of a bay wall and affect the abutting pairs of bays.

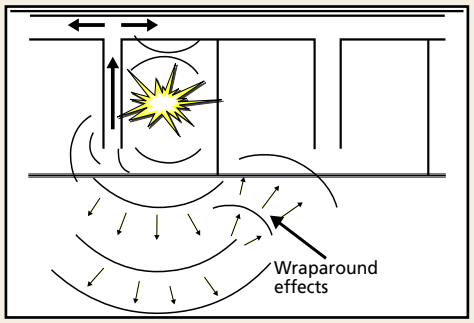

In the summer of 2004, ESA-MEE received an unprecedented opportunity to conduct full-scale safety tests at TA-16 in buildings 340 and 342 while they were being decontaminated and decommissioned. These facilities were similar in design and construction to building 260 and served as the Laboratory's HE formulation plant for many years. To support this project and collect relevant data for a number of applications, multiple organizations were involved. Thus, the project was termed

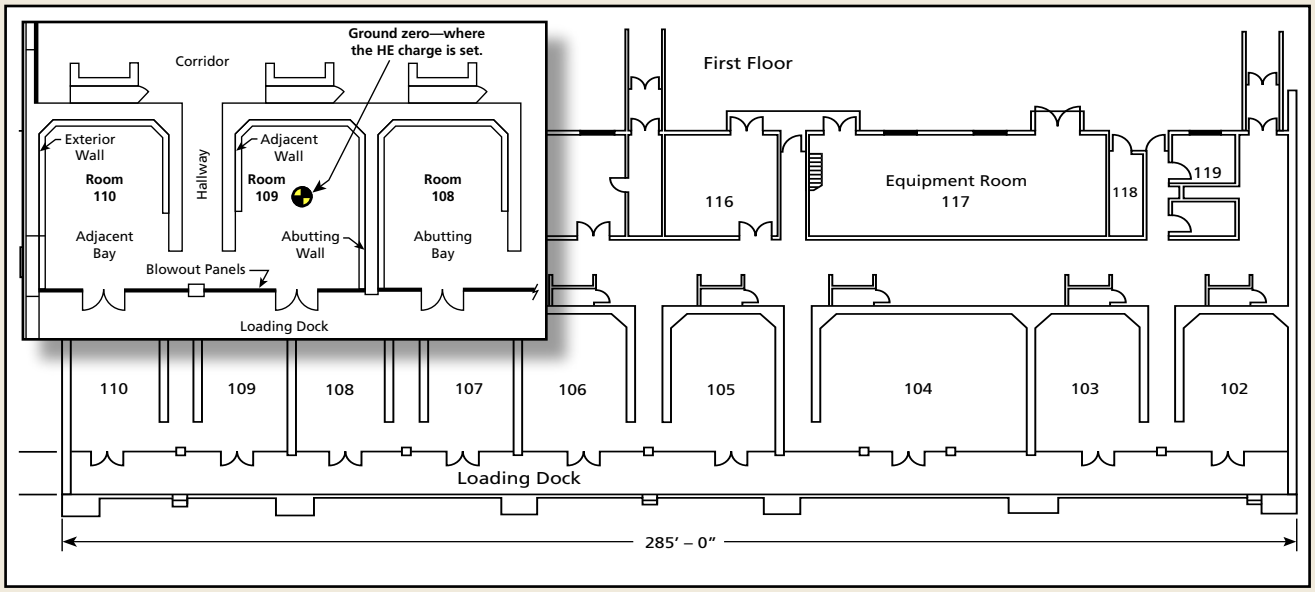

This diagram shows the layout of building 340 and its nine bays (rooms 102–110). The inset shows an adjacent bay and an abutting bay.

Joint Characterization, Analysis, and Testing conducted at the TA-16-340 complex (JCAT-340).

The objectives for the HE safety tests were to execute full-scale testing to

- qualify safety engineering controls used to mitigate a blast,
- validate HE facility design criteria, and
- validate tools used to quantify the safety margin in the DOE authorization basis.

The JCAT-340 Project consisted of 17 detonation experiments that used 0.03–300 lb of PBX 9501 within the processing bays of buildings 340 and 342. Detonation experiments at various heights and locations assessed the dynamic response of the Laboratory's HE operations buildings. The test sequence was designed to increase understanding of the potential operational safety hazards and associated physics of internal explosions, focusing on the blowout walls' and buildings' structural response.

- Blowout wall response—The 3-in.-thick blowout walls consisted of two aluminum sheets that encased insulation. Interlocking panels of this material formed the blowout walls, which were designed to protect the interior of the building from the weather, but dislodged at an applied load of approximately 1.5 psi to rapidly dissipate an explosion away from the building and its occupants. The JCAT-340 test series studied the dislodging characteristics of the blowout walls and effects of the wraparound pressure on an abutting bay. In addition, a test was conducted to reduce wraparound effects by implementing a wedge deflector to mitigate wraparound pressures. This wedge was designed to reflect the initial pressures at the end of the bay wall back into the explosives bay, thereby reducing the pressure that turns the corner and affects the abutting bays.
- Structural response—This test series was designed to characterize the structures' dynamic response (spallation, cracking, displacement, etc.) to overpressure generated by detonating HE. Buildings 340 and 342 were constructed in the early 1950s with 2-ft-thick, highly reinforced concrete walls that contained a vast web of rebar, roughly 3.5% by volume. Structural models will be calibrated from the results of a series of 5-lb test shots; larger charges were detonated to examine various structural effects.

Large hydrodynamic computational models provided the data to set the ranges on the instruments for the pressure we expected to measure during

A wedge deflector (shown at the end of the building) was used to mitigate wraparound effects in one test.

the tests and to assess the buildings' structural response. The hydrocodes CTH, a Sandia National Laboratories code, and AUTODYN, a commercial code, provided the basis for modeling.

An array of incident and reflective pressure transducers placed on the interior and exterior of buildings 340 and 342 gathered pressure data. Accelerometers, pretest and posttest forensics, and high-speed cameras captured blowout wall and structural response data. Standard and digital videos recorded detonations and provided a real-time view of ongoing events. Additionally, noise, dust, and gas meters and x-ray element analyzers assessed the industrial hygienic state of the buildings after each detonation.

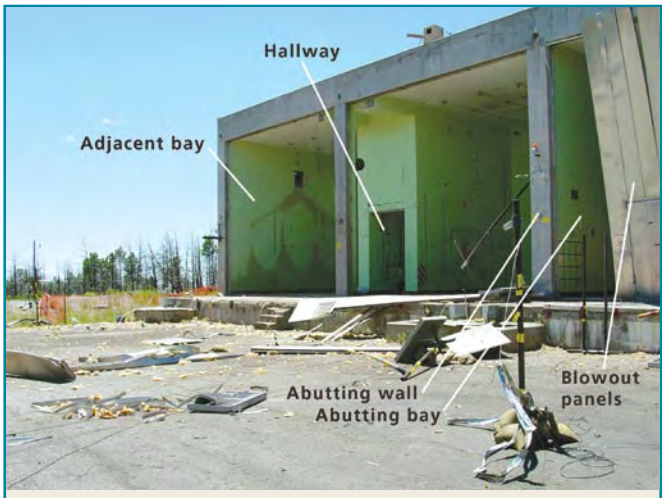

After a 25-lb test shot, blowout panels are on the ground and blowout panels in the abutting bay are damaged.

Preliminary results of the tests show five important findings.

1. The blowout walls worked as designed; they dislodged and the pressure rapidly vented from the bays.

2. Experiments in which a blowout wall was present produced significantly higher pressures and had greater structural impact from the initial shock wave reflected off the panels than did experiments without a blowout wall.

After HE pipes, fixtures, and asbestos were removed, instrumentation was attached to the exterior and interior of building 340 before a test.

Blowout panels and other debris are scattered up to 300 ft away from building 340 after a 25-lb test shot.

3. Wraparound effects seen in the 1959 accident were validated and were found to pose a significant safety concern to individuals working in the abutting pair of bays (no one works in adjacent bay pairs during HE operations because the adjacent bay is open to the working bay). The abutting bay has a 2-ft-thick wall separating it from the abutting pair of bays. Although pressures were below lethal limits for the maximum 75-lb HE operating limits, a portion of the blowout wall was thrown into the bay and could have fatally injured personnel. Fortunately, the findings from the wedge test showed that this mitigation scheme effectively reduced the wraparound pressures.

4. Blast doors effectively reduce the pressures entering the corridors from the bays, although the blast doors have the potential to fly into the corridors after an explosion. Further analysis must be conducted on a case-by-case basis because each facility has different blast door designs.

5. The building remained structurally sound to its maximum HE operating limits, and the blast was contained predominantly within the test bay. These results imply that problems relating to internal debris from concrete and piping are minimal, although loose articles or cabinets in the corridor may become falling objects.

Data from the JCAT-340 tests will be used as follows.

- ESA Division will use the data to benchmark large computational models. Computational models will then be used to assess the dynamic pressure and structural response of the HE processing bays at LANL (and possibly other DOE sites), to investigate and mitigate potential safety concerns, and to identify authorization basis siting and quantity/distance issues. Data from the experiments will also be modeled to ensure that computational results correlate to the experiment. The data should provide an accurately calibrated model to engineer an optimized and effective blast wraparound mitigation scheme for building 260, where HE operations are being consolidated.
- The Nuclear Regulatory Commission will use the data to gain further information on blast loading to highly reinforced structures such as nuclear reactors and apply the data to its empirically based computer code VISAC.
- DoD and other government agencies will use the data to develop and validate safety standards for personnel, building design for nuclear and nonnuclear buildings, and the dynamic effects on structures with respect to threat reduction.
- ESA industrial hygienists will study the particulate fallout and local atmosphere resulting from these experiments to understand and prepare for situations in which emergency personnel respond to an incident that involves explosives.

In general, data from the JCAT-340 Project may be applied to a number of computer codes, safety basis reviews, damage assessment conditions, and environmental, safety, and health applications. NWJ

Point of contact:
Daniel J. Trujillo, 665-1381, dxt@lanl.gov

JCAT-340 was headed by ESA Division and gained support from the Center for Energetic Materials and Energetic Devices, a coalition of Los Alamos, Sandia National Laboratories, and the New Mexico Institute of Mining and Technology (NMIMT) to promote and support explosives research and development. The Energetic Materials Research and Testing Center from NMIMT provided ordnance and instrumentation support for the experiments with the aid of Science Applications International Corporation. Sandia served as a conduit for the Nuclear Regulatory Commission, which supported the project financially. The ESA Weapons Operations and Infrastructure Group furnished safety personnel for the tests. LANL Project Management and Clauss Construction prepared the facility for the tests. The Los Alamos Fire Department supplied fire prevention services during testing. The ESA Weapon Response Group made modeling predictions and analyzed data. NMIMT graduate students provided test support and modeling assistance.

Successful Hydrotests Completed at DARHT

Dynamic Experimentation (DX) Division scientists at the Dual-Axis Radiographic Hydrodynamic Test (DARHT) Facility successfully completed two essential hydrotests in 2005. Hydroshots 3625 and 3612 were part of a test series designed to gather data on the LANL-developed W76 warhead, which is carried on Trident submarine-launched ballistic missiles.

Containment foam. Before the tests, technicians filled a tent-like structure with an aqueous foam to limit dispersal of materials such as beryllium, depleted uranium, and lead into the environment. Although hydrotest 3625 was a gas cavity test and hydrotest 3612 was a JOPIN test, they used similar foam containment systems to avoid contaminating the environment.

Hydrotest 3625 was conducted April 1, 2005, and hydrotest 3612 was conducted 3 months later on July 1, 2005. Results from these two hydrotests allow researchers to compare data with hydrocode predictions that eventually will be factored into refurbishment requirements for final certification of NNSA's W76 Mod 1 Life Extension Program (LEP).

DARHT is a LANL high-explosives (HE) firing site that has hydrodynamic experiment capabilities; i.e., measurements are made at the extreme temperatures and pressures generated by the detonating HE, wherein the tested metals flow like fluids. Scientists use DARHT's flash x-ray machine and cameras to study the implosion characteristics—recording interior images during implosion—of nonnuclear mockups of nuclear weapon components.

Hydrotests fall into one of two categories: joint radiograph and implosion pin (JOPIN) tests and gas cavity tests. Although DARHT can accommodate both types of hydrotests, it is the world's most capable gas-cavity test facility. LANL has conducted numerous gas cavity tests, including 3605 and 3623 (in 2004 for the W76 Mod 0 LEP) and 3625 (in 2005 for the W76 Mod 1 LEP). Recent JOPIN tests at DARHT include 3596 (in 2004 for the W76 Mod 0 LEP) and 3612 (in 2005 for the W76 Mod 1 LEP).

Gas cavity hydrotests

- have a small field of view,
- require a compact setup geometry,
- can "see through" very opaque object features that are difficult to radiograph, and
- use the gamma-ray camera (GRC) as a principal diagnostic tool.

JOPIN shots, which do not require the full radiographic intensity of DARHT,

- have a very large field of view,
- can "see through" transparent object features that are easily radiographed,
- are concerned with case and other device components,
- diagnose early-time implosion with pins, and
- use many different diagnostics.

The manufacture of some W76 replacement components, scheduled to begin in late 2006, will be based in part on the results of the DARHT W76 test series. Before manufacturing begins, LANL will conduct confirmatory experiments to ensure that the new components perform as well as those built

for the test series. Meanwhile, LANL scientists are comparing radiographic, pin, and other data from previous hydrotests (e.g., 3605 and 3596) with data from hydrotests 3625 and 3612. All these data are used to refine existing computer models and to analyze hydrodynamic performance. NWJ

Points of contact:
Scott Watson, 665-6233, scottw@lanl.gov
Lori Primas, 665-4794, lorip@lanl.gov

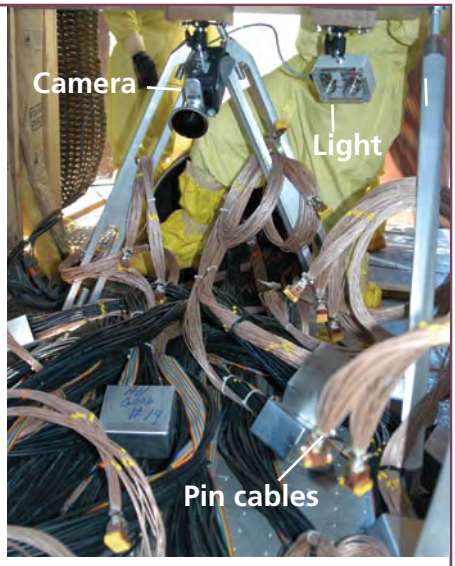

Pin harnesses for hydrotest 3612. Diagnostic tools for shot 3612 included several hundred precisely aligned electrical pins that measured the contours of the imploding components, high-explosive microwave detectors, an electronic framing camera, pressure sensors, contact switches, and thermocouples. Radiographic images were recorded on film and phosphors.

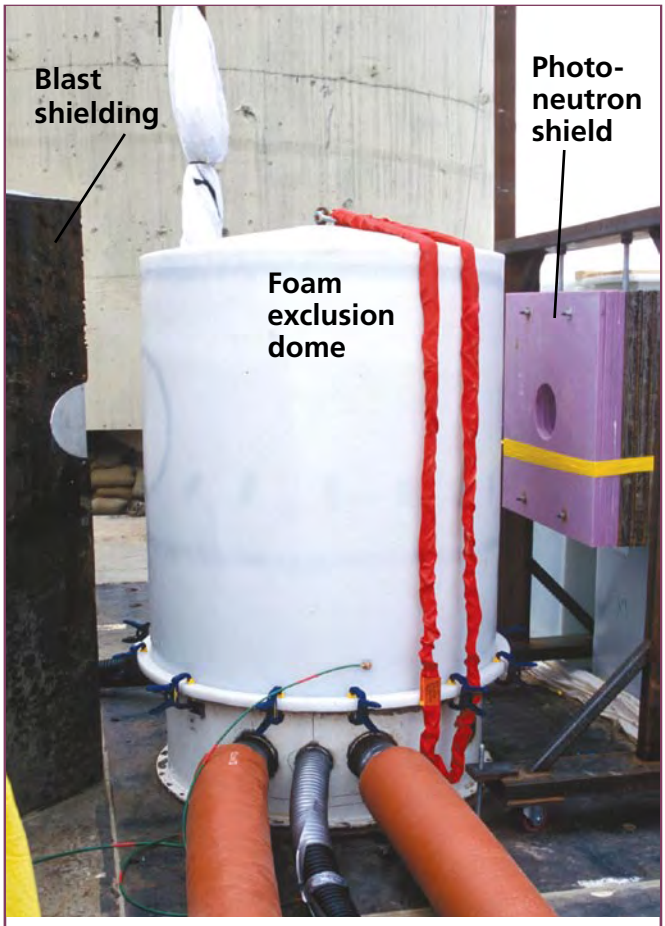

Foam exclusion dome. To avoid exposing test components to the containment foam, DX personnel sealed all 3612 and 3625 components in a container similar to this one used for shot 3605. Red strapping cables were used to emplace the dome; the two red cables at bottom protected pin harnesses from the containment foam after emplacement.

Hydrotest 3605. Sequential outside views show the two axes and containment tent before detonation *(upper left)*, approximately 1 s after detonation *(upper right)*, approximately 5 s after detonation *(lower left)*, and approximately 20 s after detonation *(lower right)*.

Modeling Coupled Fluid-Solid Response in Low-Density Cellular Material Systems

Theoretical Division scientists have developed a promising new approach to modeling the dynamic response of cellular materials. Using this innovative methodology, we now consider the coupled physical response of both a cellular solid and a permeating fluid in a comprehensive, continuum-scale description for cellular material systems. This approach quantifies the influence of a permeating fluid (e.g., air or water) on the 3-D deformation of a cellular solid (e.g., polymeric foam or wood) and the influence of a deforming cellular solid on fluid transport through the corresponding cellular structure. This approach also allows investigators to distinguish between the physical mechanisms and material response characteristics that are due to solid material response and those that are due to the physical behavior of the permeating fluid.

The purpose of our investigation is to

- identify the role of fluids in the overall response of cellular material systems,
- show that previous modeling efforts neglected relevant physical behavior, and
- provide an effective approach to modeling cellular materials systems.

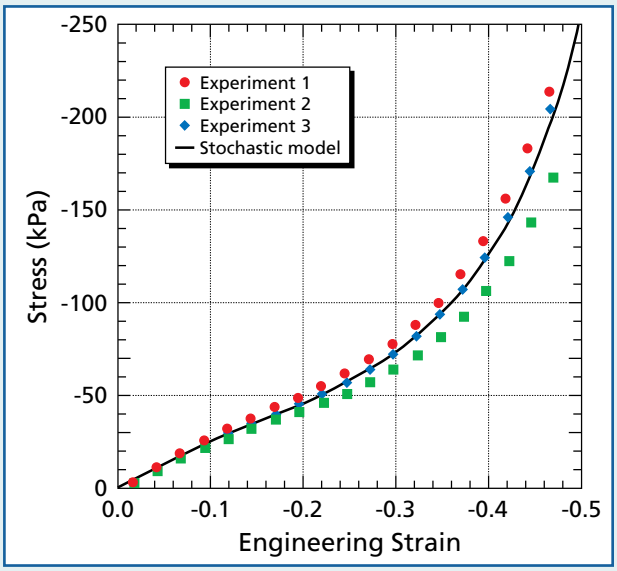

Continuum-scale, stress-strain response. Three silicone foam samples were subjected to uniaxial compression. Each sample was a highly disordered, open-cell silicone foam with identical average material properties. LANL scientists used a stochastic constitutive model to simulate the response of this material to quasi-static loading conditions. For the uniaxial deformations considered here, engineering strain is directly related to the ratio of compression (i.e., the length of the compressed specimen divided by the original length).

Multifield Approach

This new modeling approach is based upon a multifield (i.e., a cellular solid and a permeating fluid) description of the governing equations of motion. Multifield theory is applicable when the average motion of one material in a multimaterial system is distinctly different from that of the other materials. Examples of such systems are gas bubbles in water and fluids flowing through porous or cellular solids. Before we developed this method, a multifield approach had not been used to describe the dynamic response of cellular material systems, despite the applicability of multifield theory to the dynamics of flexible foams.

The multifield formulation begins with the assumption that cellular materials are composed of two separate but interacting material fields: a cellular solid (e.g., polymer in a foamed state) and a permeating fluid (usually air). In general, the motion of the two material fields is not identical but is coupled through relative motion.

The response of each material is characterized by its own distinct velocity field, while the response of the overall cellular material system is governed

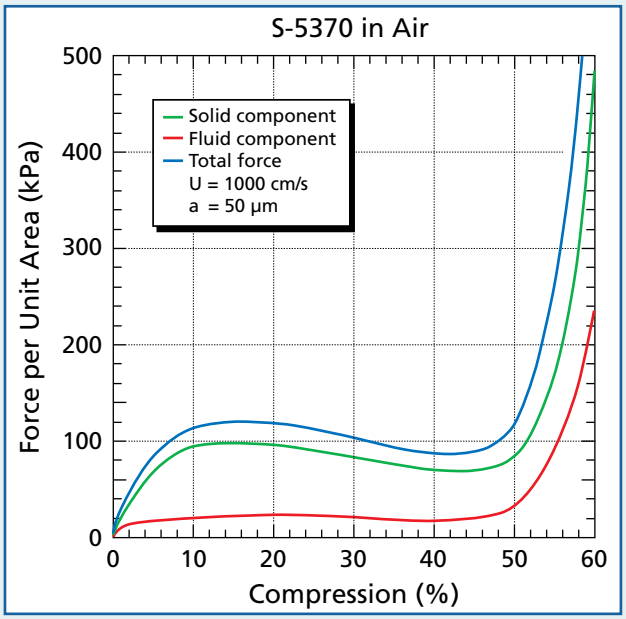

Total force per unit area. The force required to move a piston at constant velocity is plotted as a function of uniaxial compression, and the total force is decomposed into solid and fluid components. Prescribed boundary conditions allow outflow of the permeating fluid at the stationary wall, where the cellular solid is constrained to zero velocity. The moving piston compresses the cellular material, forcing the permeating fluid through the cellular structure (U = piston velocity, a = aperture size). A rapid increase in total force at the highest compression levels coincides with the return of the cellular solid stress wave to the piston boundary, compressing the solid to nearly full densification. The cellular solid then compresses the permeating air, which is restricted from flowing freely through the small apertures between cells, producing a significant corresponding rise in fluid pressure.

by a set of coupled conservation equations for mass, momentum, and energy. To derive multifield conservation equations, we used a traditional ensemble-averaging technique (i.e., a theoretical averaging technique involving all possible material states) and developed models for the additional momentum and energy source terms that arise through the averaging process.

We used this multifield approach and a stochastic constitutive (i.e., stress-strain) model for the cellular solid to simulate the dynamic response of highly disordered, open-cell silicone foams to dynamic loading conditions. The material studied is a low-density structural foam (S-5370) used primarily to manufacture stress cushions that are designed to protect stiffer metallic parts in multicomponent engineering systems. The parent solid is polydimethylsiloxane (PDMS) reinforced with silica particles, and the foam is produced in a hydrogen blowing process. In an undeformed configuration, this material is 66% air by volume. Thus, typical of this class of materials, the foam is lightweight and soft relative to its parent solid.

To solve the equations of motion, we used a conventional, finite-volume computational algorithm in which multifield conservation equations are solved in a reference frame that moves with the velocity of the cellular solid (i.e., the Lagrangian frame), while the permeating fluid is allowed to flow through this frame with a different velocity. We updated

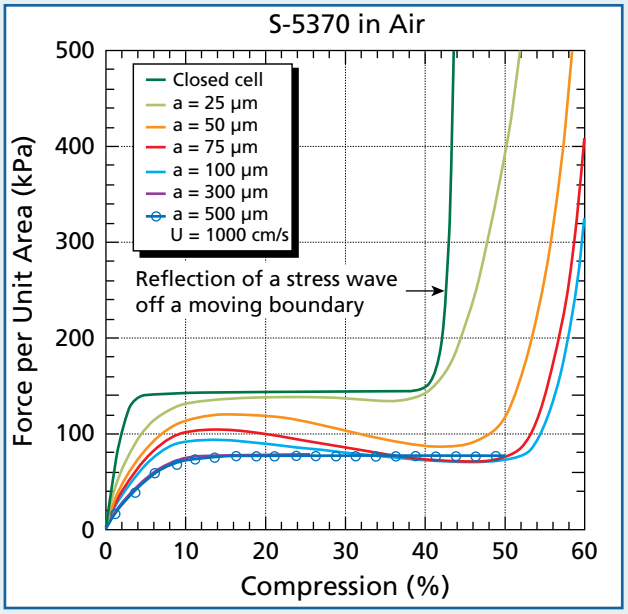

Effect of aperture size. When aperture size (a) increases, fluid pressure rises as the force required to move the piston decreases. For a closed-cell foam, the responses of the cellular solid and permeating fluid are fully coupled, constraining the motion of each field to the same average velocity. When apertures are larger than approximately 300 μm in diameter, the responses of the two fields are fully uncoupled and the permeating fluid no longer contributes to the total force on the piston. For 0- to 300-μm-diameter apertures, the microstructure (aperture size) and coupling of the permeating fluid behavior with the cellular solid response affect signal propagation speeds. Maximum loads occurring in the force-compression response curves, variations in the compression levels at which they occur, and compression-level variations corresponding to a rapid increase in piston force show that the cellular solid stress wave and fluid pressure wave travel at different velocities (U = piston velocity).

the average stress state in the cellular solid using the stochastic constitutive model and repeated the incremental solution procedure until the foam sample reached a predetermined level of macroscopic compression.

Our simulations are the first to combine advanced constitutive models for a cellular solid with a physical representation of the associated permeating fluid behavior in a comprehensive continuum-scale response description for cellular material systems. Our results show that the permeating fluid may strongly influence the general response of cellular material systems, contributing to the overall load-carrying capacity of the material and affecting rate dependence and signal-propagation speeds. Our data also show the usefulness of the multifield representation and suggest that any modeling approach developed for cellular materials must account for pressure evolution and flow behavior of the fluids present in cellular material systems.

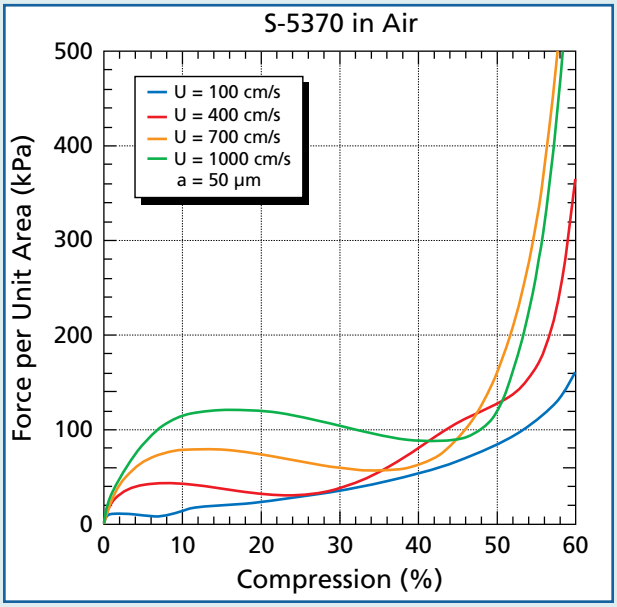

Effect of loading rate. A piston velocity (U) of 100 to 1000 cm/s is used for loading. As loading rate increases, the force required to move the piston generally increases. However, at compression levels higher than approximately 35%, the cellular solid stress wave and the permeating fluid pressure wave propagate at different velocities. The pressure wave in the permeating fluid travels at a higher velocity and out of phase with the cellular solid stress wave, leading to nonmonotonicity (i.e., force does not necessarily increase with compression but can decrease) in response to higher compression levels. However, because the stochastic constitutive model is elastic, rate effects exhibited in these simulations are due solely to the coupled behavior of the permeating fluid (a = aperture size).

This multifield approach to modeling cellular material systems allows researchers to identify the materials, applications, and conditions under which a permeating fluid affects the response of a surrounding cellular solid and to distinguish between the physical mechanisms associated with each distinct material field. For example, with our approach, researchers can differentiate between the effective system stiffness associated with a cellular solid stress state and the stiffness resulting from developing pressures in a permeating fluid. Likewise, rate dependencies related to viscoelastic properties of a solid can be differentiated from rate dependencies related to viscous mechanisms associated with the flow of a permeating fluid through a cellular structure. These distinctions lead to a more physically based modeling approach—rather than purely phenomenology-dependent constitutive models—and an improved predictive capability for cellular material response simulations.

Insight into the coupled fluid-solid response of cellular material systems allows researchers to identify materials and conditions that are significantly affected by a permeating fluid and applications for which a typical single-field description of cellular-solid response alone is inadequate.

Future Research

Future LANL research into cellular material systems will focus on generalizing our multifield approach to better describe relevant physical mechanisms for both fluids and solids. We will include models for flow separation, viscosity-induced shear stress, and turbulence-induced Reynolds stress in the permeating fluids, as well as models for viscoelasticity and friction in the cellular solid. Problems of interest will include elastic wave propagation, low-frequency vibrations, sound-wave attenuation, and strongly dynamic, shock-inducing phenomena. NWJ

Point of contact:
Mark W. Schraad, 665-3946, schraad@lanl.gov

Moore T-Base Lathe Retrofit for Beryllium Machining

The need to upgrade a T-base lathe control system no longer supported by its manufacturer provided an opportunity to enhance the capabilities of the Moore lathe used in the Beryllium Technology Facility. The enhancements, developed by collaborations between Manufacturing Systems and Methods (MSM) Division's Manufacturing Capability Group (MSM-5) and Manufacturing Technologies Group (MSM-6), allow machinists to monitor the nonnuclear weapon component machining process without removing the fabricated parts from the machine. These improvements benefit both the Pit Manufacturing and Certification Program and the Experimental Hydrodynamic Test Program by reducing component manufacturing time and eliminating in-process handling that could damage parts.

Moore T-base lathe with unclassified part. The retrofit of a Moore T-base lathe completes the first phase of a collaborative project that reduced security risks by eliminating classified computer disks and shortened in-process inspections from hours to minutes.

These MSM-developed technologies—already successfully deployed on other LANL machining platforms—also eliminate classified removable electronic media (CREM) associated with machining processes, reduce manufacturing time, and increase machine usability and operational efficiency. The upgrades, completed in January 2005, include

- remote boot capability for diskless operation, which eliminates CREM-related security risks;
- a modern computerized numerical control (CNC) controller that ensures software compatibility, standard personal computer (PC)-operator interface and Ethernet link, and the look and feel of other controllers the Laboratory uses;
- quick-change fixture couplings that allow machinists to change precision fixtures in seconds instead of tens of minutes;
- in situ contour probing, which reduces in-process inspection time from hours to minutes and virtually eliminates the risk of damaging fabricated weapons components; and
- an MSM-designed optical tool locator system that allows the use of industry-standard cutting-tool inserts that extend tool life, improve surface-finishing capabilities, reduce waste, and cut costs.

Modern CNC Controller

The Fanuc 160i controller, the model used on most machining platforms that the Laboratory has purchased within the past few years, was selected for this retrofit. Although standardizing all Laboratory lathe controllers is impossible, limiting the number of manufacturers improves operational and maintenance commonality, which reduces operator training needs.

Unlike "open architecture" controllers that employ one central processing unit that performs all control functions (servo loops, programmable logic controller sequencing, and operator interface), the Fanuc 160i provides end-user flexibility through standard operator interface with a high-speed communications link. This PC-Ethernet connectivity allows the machinist to access a parts database directly from the controller. Access to this database eliminates

the need for intermediate computer platforms on the shop floor and a distributed numerical control system for file transmission.

Quick-Change Fixture Couplings

Hydraulic drawbar systems that are standard equipment on modern CNC equipment have enabled the use of curvic couplings. These couplings allow a machinist to change high-precision fixtures within seconds while ensuring that they are correctly aligned to both the spindle rotation and z axes. To change a fixture before the retrofit, the machinist bolted the fixture to the spindle face and using a dial indicator and a mallet, centered the fixture on the spindle face—a tedious and time-consuming process.

Contour Probing

Characterizing the triggering response of the probing system using a toroidal (doughnut-shaped) calibration artifact and software developed by MSM-5 engineers, the new contour probing system virtually eliminates the need for in-process inspection of the component shell. Because the machinist can measure a component without removing it from the machine, the new system significantly reduces the time needed to ensure accuracy during the machining process. It also eliminates health and safety hazards and damage to the component that were associated with manually inspecting and reinstalling the component.

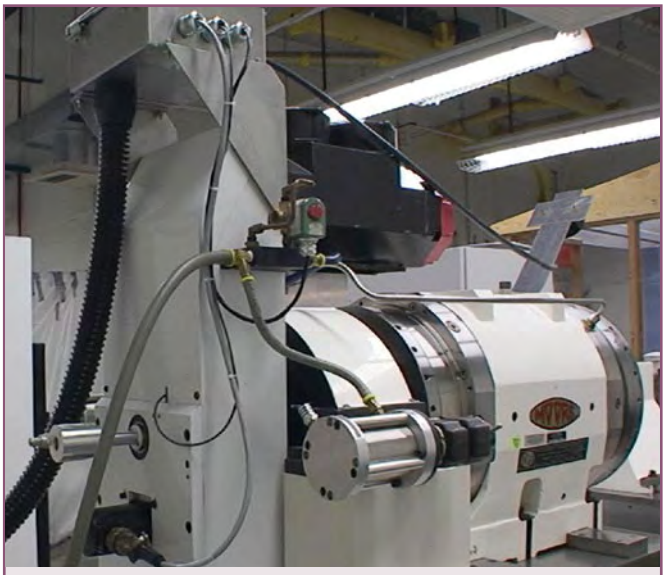

Spindle assembly (rear view). The Moore T-base lathe originally was configured with a hollow-shaft spindle motor through which the vacuum source for holding the part passed to the face of an air-bearing spindle. With this spindle motor configuration no longer available as a stock item, MSM engineers designed a new spindle drive package to accommodate the use of an off-the-shelf spindle motor. The design included equipment required for C-axis (spindle positioning) capability, which in turn enabled the installation of curvic couplings and a part probing system.

Curvic coupling. MSM's innovative designs enabled the use of curvic couplings, which are highly accurate and reduce machine setup time. This technology has been implemented in other high-hazard Laboratory operations.

Cutting-Tool Inserts

Recent industrial advances in cutting-tool technology have extended tool life, reduced machining time, and improved surface finishing by orders of magnitude. These more-effective cutting tools (inserts) are inexpensive, provide multiple cutting surfaces, and produce smaller waste streams. Utilizing the manufacturers' advanced technology ensures continuous improvement and enhanced performance in the fabrication of nonnuclear weapon components—without arduous LANL testing.

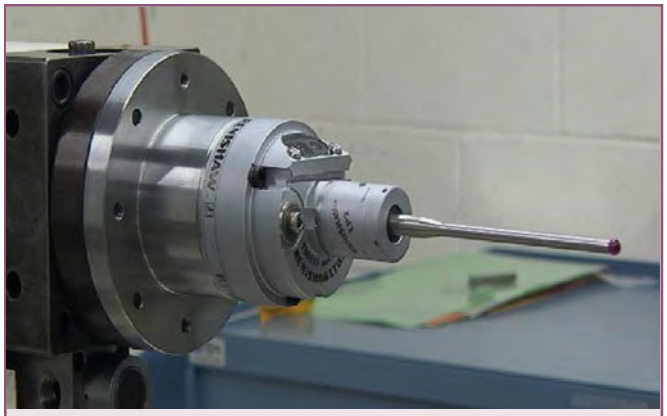

Renishaw LP2 probe. Using standard off-the-shelf hardware, MSM engineers and machinists designed software that measures components during the machining process, eliminating the need for manual part removal, inspection, and reinstallation. Using on-machine probing reduces the risk of handling errors that result in damage to component parts.

One downside to using these inserts rather than custom-ground tools is that manufacturers cannot hold the size of a tool nose radius to a specific value. Also, using stock equipment and traditional methods, the high rake angles required for shearing and chip control make it difficult to position the tool relative to the centerline of the spindle. In general, however, in terms of lower cost and efficiency of operation, the benefits of using these inserts outweigh their limitations.

Optical Tool Locator

To mitigate the drawbacks of mass-produced cutting-tool inserts, MSM-6 machinists and MSM-5 engineers developed an optical tool locator that can

1. characterize the radius of the tool tip without touching the tool, the component part, or the fixture and

2. position an insert in all three axes (i.e., points in space) relative to the coordinates of the machine (the traditional contact probe accommodated only two axis settings).

With this system, a machinist can change an insert very late in the fabrication process even if the inserts vary in size. Software integrated into the PC at the machine controller automatically updates the cutting-tool offset registers to compensate for wear on the cutting tool or variations in the nose radius.

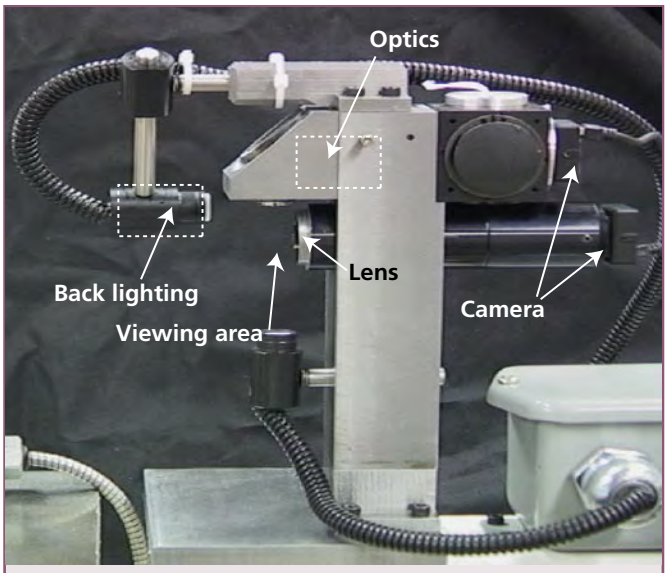

Optical tool locator. MSM machinists and engineers devised a multifunctional tool locator that characterizes and orients the cutting insert during fabrication. Imaging the tool in two views, the locator correctly positions the insert and automatically updates the lathe's cutting-tool registers.

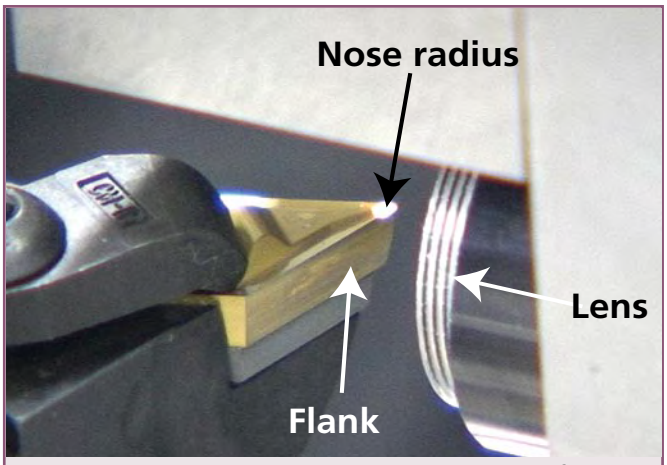

Cutting-tool insert. The numerous advantages of using industry-developed cutting tools (inserts) to fabricate nonnuclear weapon components include reduced cost, extended tool life, better chip control, less machining time, less waste stream, and improved surface finishing.

The successful T-base lathe retrofit resulted in a system that has a proven track record for safely and accurately machining beryllium for nonnuclear weapon components. MSM-devised enhancements (precision couplings, optical tool locator, and contour probing) that utilized commercially available cutting tools, combined with the newly installed Fanuc 160i controller, ensure LANL operates the most capable and flexible T-base machining platform in the Nuclear Weapons Complex. NWJ

Point of contact:
Jody Niesen, 665-1693, niesen@lanl.gov

Definitions

curvic coupling—Precision mechanism used to locate and position mechanical assemblies.

fixture—Used to hold parts during fabrication.

hydraulic drawbar cartridge—Mechanism that generates the force that holds material in place during fabrication.

optical tool locator—Device that uses optical images to characterize a cutting tool.

part—Finished product (component) of the machining process.

rake angle—Angle of the insert tip.

trigger response—Mechanical characterization of probe system switches.

Atlas Generates Success at the Nevada Test Site

Atlas is the world's first pulsed-power system designed specifically to use electromagnetic drive (magnetic fields produced by large electric currents) to perform high-precision experiments that explore the properties of condensed matter and the behavior of complex hydrodynamic geometries. Electromagnetic drive naturally and conveniently produces cylindrical implosion (like the traditional "z-pinch." In "z-pinch," a powerful axially directed ["z"] current produces azimuthal magnetic fields that squeeze the conductors carrying the current toward the center).

Implosions automatically produce the multidimensional effects in materials that are important to understanding material behavior in nuclear weapons. Electromagnetic drive from Atlas enables scientists to characterize the behavior of materials at the extreme conditions present in an operating nuclear weapon. Data from such experiments are needed to validate the computer codes that scientists rely on to certify US nuclear weapons in the absence of underground testing.

Designed and built at Los Alamos, Atlas was moved to the Nevada Test Site (NTS) beginning in late 2002. Reassembly was completed in April 2004 and testing began in May, but was interrupted in mid-summer 2004. Restart activities were completed in April 2005 with a successful full-system test in which Atlas' pulsed-power discharge delivered in excess of 23 MA (million amperes) to a fixed-inductance test load. The full-system test marked the return of Atlas to operational status and allowed resumption of pulsed-power characterization testing involving approximately 16 separate tests in a variety of machine configurations and with two static loads. Characterization testing was completed in July 2005.

The Atlas pulsed-power machine was relocated to NTS to continue its mission of providing physics data for use in developing and validating new weapons materials models and computer codes. The Marx generators are in maintenance units in the outer ring of Atlas. An experiment would be located at the center of the assembly.

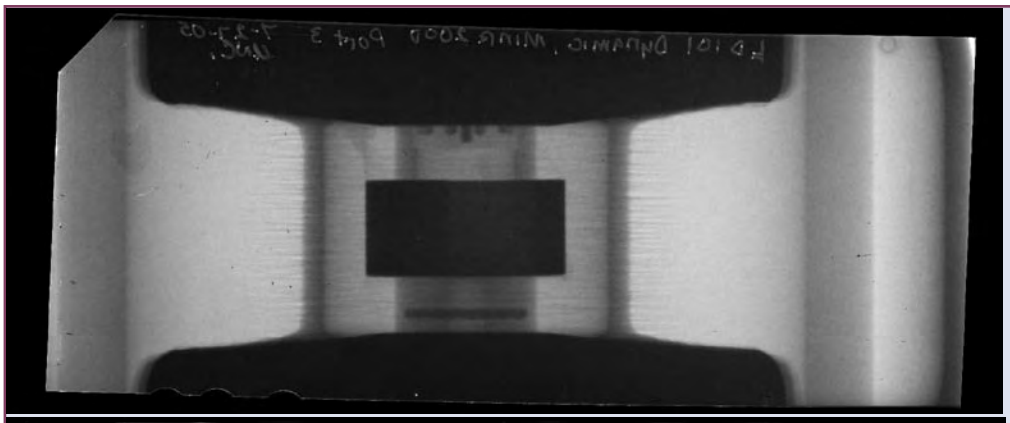

LD-101 indicated perturbation growth, seen as a rippling on the back surface of the liner and as dark horizontal stripes on the radiograph, occurred at the driving interface between the magnetic field and the liner surface.

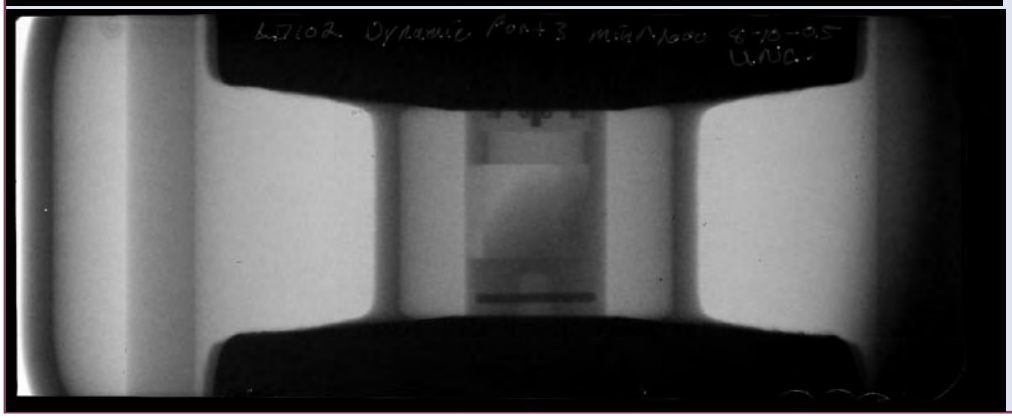

LD-102, conducted at lower drive current, showed no indication of perturbations—providing important information about the instability growth process in imploding liner systems.

Since the completion of characterization testing, four successful physics experiments were conducted on Atlas at 2-week intervals—July 27, August 10, August 25, and September 8, 2005.

A Los Alamos-Bechtel Nevada (BN) team conducted the first Atlas implosion physics experiment at NTS on July 27, 2005. Atlas delivered the planned 19 MA of electrical current to a 68-g aluminum cylindrical shell, or liner, about the size and shape of a tuna can. The experiment had two objectives: (1) to demonstrate that Atlas is ready to conduct physics experiments and (2) to continue LANL's ongoing investigation of instability physics in imploding liner systems. The two-shot Liner Demonstration (LD) series proved that Atlas was ready to support research for certification of the nation's nuclear weapons stockpile and met an NNSA FY05 Level 2 milestone.

The diagnostic suite fielded on LD-101 included the following.

- Three channels of transverse radiography demonstrated excellent liner implosion performance. The superior resolution of the radiography showed early indications of perturbation growth (rippling) on the back surface of the liner. Understanding perturbation growth is important for future experiments because departures from near-perfect symmetry and uniformity in the liner implosion may result in nonuniform or complex conditions in the target that obscure the fundamental physics objects of the experiment.

- Velocity interferometer system for any reflector (VISAR) measurements that tracked the inner surface velocity of the liner confirmed the liner performance observed with radiographs.

- High-precision current measurements using the Faraday rotation technique (an optical technique for measuring very large currents using fibers in place of metal conductors) provided the detailed drive data needed to correlate measured with simulated liner performance.

- Electrical measurements of pulsed-power system performance confirmed that Atlas operated as designed.

LD-102, the second implosion physics experiment in the LD series, was conducted on schedule, 2 weeks after LD-101. LD-102 had two objectives: (1) to demonstrate that Atlas can conduct physics experiments at 2-week intervals and (2) to continue the investigation of instability physics in imploding liner systems, specifically by changing the drive conditions to explore perturbation growth.

The diagnostic suite for LD-102 was similar to that for LD-101. All critical diagnostics delivered good data. LD-102 explored liner performance at lower current delivery (more-gentle drive) than LD-101. Under reduced drive, enhanced instability might (by some models) have been expected. However, radiographs showed no evidence of increased instability at the lower drive achieved in LD-102 in agreement with previous Atlas experiments at LANL.

Throughout the LD series, shot operations became smoother and more efficient, indicating that the Atlas system was successfully relocated and that the new BN operating team was rapidly gaining experience with the pulsed-power operating environment. Preparation for the next experiments (Spall) required some minor changes in machine configuration, installation of the spall target assembly, and some additional diagnostics, which made the prompt execution of the first Spall test another notable accomplishment.

Two material damage experiments, Spall 101 and Spall 102, were conducted on August 25 and September 8, additionally demonstrating that the Los Alamos-BN team can set up and conduct implosion liner experiments on a 2-week schedule.

The Spall test series is designed to provide detailed information about the formation and evolution of damage in a well-characterized reference material (aluminum) using the converging geometry characteristic of the operation of a nuclear weapon. Spall experiments on Atlas at NTS continue the experimental series begun in 2002 when Atlas was located at Los Alamos. After benchmarking the results of the NTS Spall experiments against data collected using the same techniques and parameters in Los Alamos, the series will explore recollection and

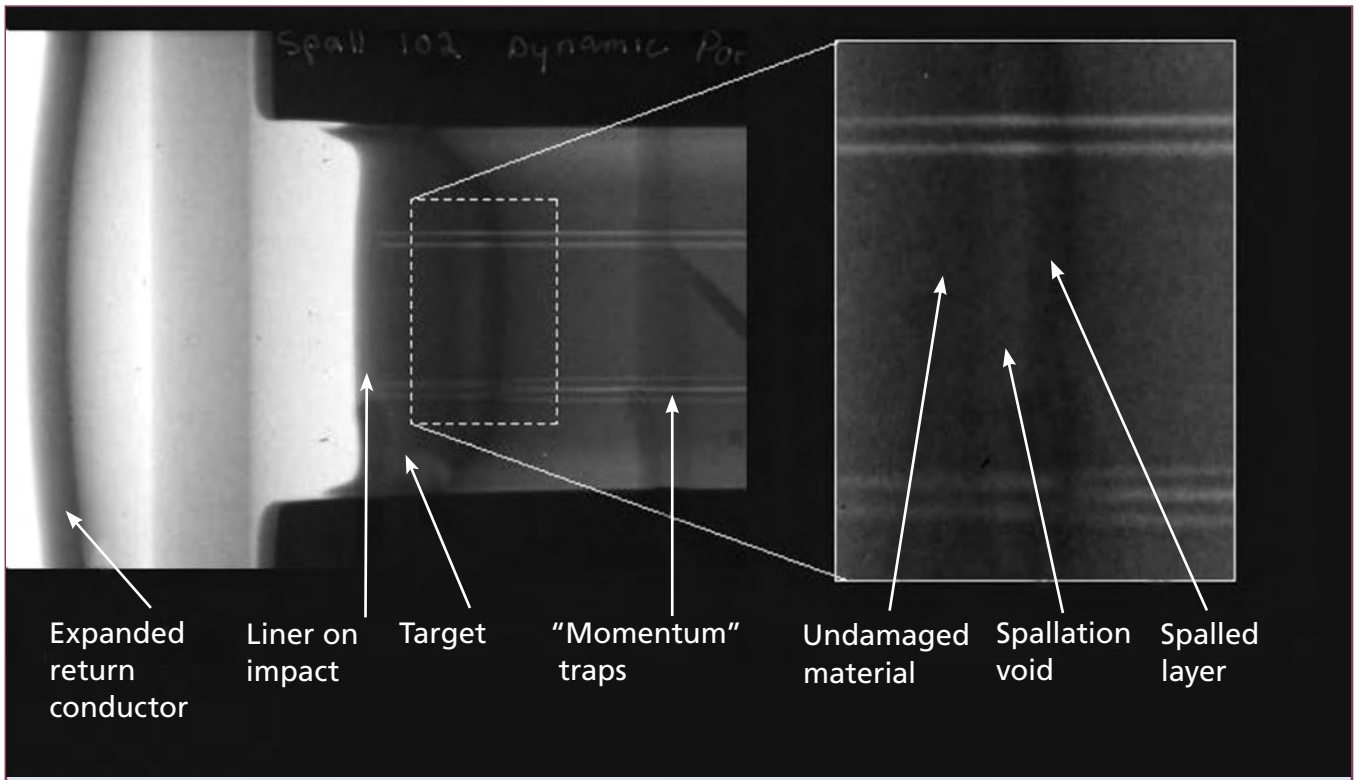

Samples recovered after Atlas experiments allow post-shot metallurgy to explore structure of material after it has been strained (deformed) beyond failure. Both spall layer and undamaged material show residual evidence of significant distention and void formation prior to failure instead of a clean, sharp break.

compaction of damaged material. Cylindrically converging geometry is particularly well suited for these experiments because the interface between the damaged and undamaged material is continuously accelerated. Under these conditions, the undamaged material can overtake (catch up with) the damaged material ejected earlier in the implosion, first sweeping up the damaged material (recollection) and then pressing it together (compaction) with enough force to possibly fuse the recollected material once again into a solid layer. Pulsed-power techniques apply the precise, controllable, time-varying acceleration to the surfaces that is needed to study these phenomena with much more controllability, flexibility, and reproducibility than is available from cylindrical high-explosives systems. In the nearest future, some spall experiments may also be conducted on other pulsed-power systems to allow a range of high-priority experiments to be promptly conducted on Atlas.

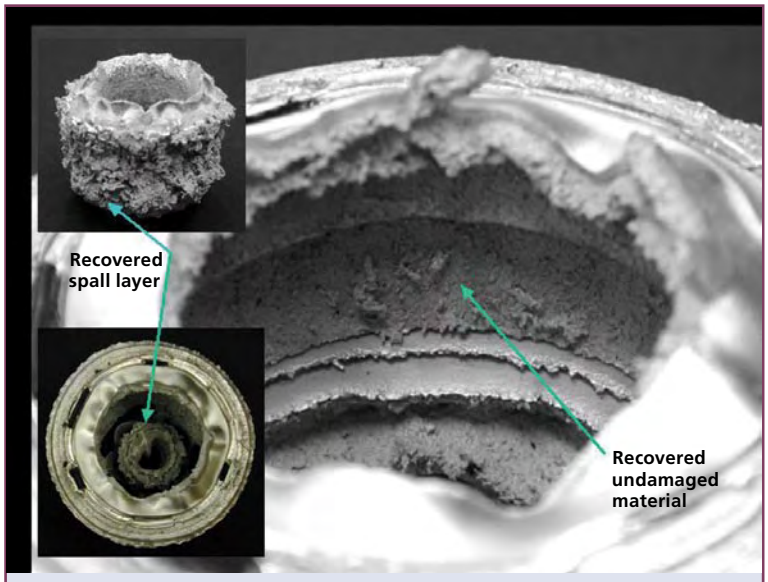

Radiograph from the Spall 102 experiment captures the spalled layer after it separates from the undamaged material. The free-flying layer decelerates because there is residual strength in the complete, spalled cylinder, bringing the free-flying layer to a stop and allowing subsequent recovery.

The principal objectives of the first two Spall experiments, performed at approximately 60 kb shock pressure, were to reliably recover both undamaged and spalled material for post-shot metallography, remove an ambiguity in breakout velocity remaining from VISAR measurements conducted at LANL, improve the fidelity of radiographic imaging during and after the spallation process, and begin exploring the effect of plastic work (deformation during the implosion process) as a mechanism for dissipating energy in the converging shockwave that produces the spall. The spalled layer was recovered intact in both Spall 101 and 102 experiments, having been halted in flight largely due to strength operating in the cylindrical layer. The undamaged target material behind the spalled layer was similarly recovered for post-shot metallography. Dual interferometric techniques applied in the VISAR measurements successfully removed the ambiguity in breakout velocity measurements, providing good agreement between calculated and measured values. Significant improvement in radiographic imaging was demonstrated with the free-running, spalled material clearly identifiable in the post-spall radiograph on the Spall 102 experiment. An open (void) region between the undamaged and spalled layers was clearly visible. Spall 102, with its thinner target, was capable of dissipating less energy by plastic work before spalling and provided good data for future comparison.

Data obtained in the unique implosion geometry produced by Atlas are used to validate computer codes and the analytical and numerical models used in stockpile certification studies. Atlas supports the DOE Stockpile Stewardship Program as part of a tri-lab (Los Alamos, Lawrence Livermore, and Sandia National Laboratories) resource. NWJ

Points of contact:
Janet Neff-Shampine, 667-8214, neff@lanl.gov
Bob Reinovsky, 667-8214, bobr@lanl.gov

Principal investigators for this project were Ann Kaul of the Plasma Physics Group (X-1), George Rodriguez of LANL's Center for Integrated Nanotechnologies, and Walter Atchison of X-1.

Characterizing Beryllium as a Capsule Material for Inertial Fusion

A principal goal of the national Inertial Confinement Fusion (ICF) Program is to achieve thermonuclear ignition in the laboratory using deuterium-tritium (DT) fuel. Using LANL-designed shock-wave experiments, we will understand and control instability-seeding mechanisms. Through continuum mechanics simulation studies and laser experiments at the National Ignition Facility (NIF), we hope to demonstrate the ignition of a thermonuclear burn wave in DT fuel contained in a target that we will implode with a pulse of laser energy. The effectiveness of the implosion will be indicated by energy gain, i.e., how much more energy the implosion produces than the NIF lasers supply.

At thermonuclear ignition, the fuel capsule has been imploded by a factor of approximately 30. Irregularities grow through Rayleigh-Taylor instability, and ignition may fail if the perturbations are large enough to mix large amounts of capsule material with the fuel or if the necessary compression and hot spot temperature are not achieved. At left is a polished fuel capsule; an x-ray phase contrast radiograph shows apparently high smoothness (*center*). A simulation of the imploded capsule around the time of ignition shows the growth of small irregularities to form large bubble-and-spike structures (*right*). Specifications on surface uniformity have been developed using radiation hydrodynamics simulations of the effect on thermonuclear yield. For example, the outside of the beryllium capsule must be smooth to within 3 microns, the capsule thickness must be uniform to within 0.5 micron, and the DT ice layer must be uniform to within 1 micron.

Several different ignition target designs are being developed. The most promising is an LLNL-LANL design that uses laser energy to heat a hohlraum—the interior walls of a cavity that contains the capsule. The hohlraum smoothes out spatial irregularities in the laser beams; the resulting soft (poorly penetrating) x-ray radiation implodes a spherical capsule containing DT fuel. The fuel is in the form of a layer of ice, under pressure and cooled cryogenically. The fuel capsule is designed to absorb energy from the hohlraum's radiation field without allowing x-rays to heat the fuel, because heating would make the fuel more difficult to implode and ignite.

The best x-ray absorbers for this purpose are elements with low atomic numbers, as they allow the x-rays to penetrate the DT fuel capsule wall, heating it until it explodes (ablates), and pushing the remaining capsule material and fuel inward.

The preferred capsule material is beryllium, with percent-levels of copper added to reduce heating by higher-energy x-rays. Beryllium's density, high compared with that of alternatives such as plastics, improves its performance as an ablator. Beryllium's relatively high thermal conductivity helps keep the fuel temperature uniform, which in turn helps maintain uniformity in the DT ice thickness.

NIF Experiment

In the NIF experiments, the ignition capsule will implode by a factor of approximately 30 in radius. This is a relatively high convergence ratio, and any spatial variations in radiation drive, capsule thickness, surface finish, or material properties cause perturbations that magnify greatly during implosion, principally by the ablative Rayleigh-Taylor instability. Perturbations turn into bubble-and-spike structures that break up the capsule shell and DT ice layer, reduce compression, and pollute the fuel with capsule material. Perturbations with an approximately 50-μm wavelength grow most rapidly in this proposed ignition design.

Like almost all metals, beryllium is crystalline: the capsule will be composed of many small crystals with different orientations. In beryllium, the response of each crystal to heating and compression is anisotropic, i.e., different along different crystal directions. The combination of x-ray heating and compression caused by material ablating from the outer part of the capsule can potentially cause fluctuations in pressure from the crystals' anisotropic response. Smaller crystals should induce smaller perturbations, so we could specify that the capsule material comprises crystals that are sufficiently small. We also could melt the beryllium rapidly with x-rays or shock heating. However, in both cases the properties of beryllium—on the few-nanosecond time scales and loading conditions of the NIF capsule—are not established well enough that we can specify the capsule's crystal structure or heating and loading conditions.

Ablator Characterization

The ablator characterization project, involving staff from LANL, LLNL, and SNL, and experiments at SNL's Z accelerator, LANL's Trident laser, and the University of Rochester's Laboratory for Laser Energetics (OMEGA), will (1) establish the shock pressure required to melt beryllium and (2) determine the pressure and velocity perturbations created during heating and compression. Our strategy is twofold: first, unravel the basic properties of beryllium crystals, and second, use a combination of beryllium capsule simulations and experiments to predict and verify constraints on crystal size and orientation (microstructure) of the capsule to control implosion instability.

Conditions we will explore include compression to several million atmospheres (hundreds of gigapascals) and heating to several thousand degrees kelvin in nanosecond time scales. Microstructural properties include

- the relation between pressure, compression, and temperature (known as the equation of state, or EOS);
- the parameters that describe the elastic deformation of a crystal in each direction during compression and heating (the elastic constants);

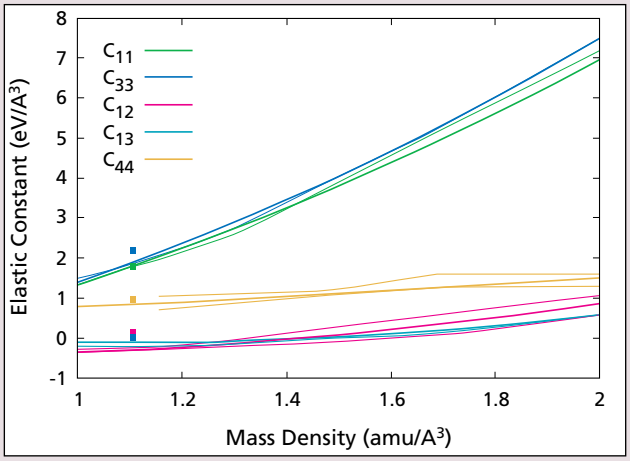

Elastic constants for beryllium. The graph shows quantum-mechanical predictions (thin lines) and quadratic fits (thick lines) for each elastic constant, together with measured values at STP.

- the rate at which plastic flow counteracts elastic deformation, as a function of compression and temperature; and
- the locations of any phase transitions (in pressure and temperature, including the melting transition) and the rates of transformation.

Theoretical Predictions

In principle, beryllium's response to compression, deformation, and heating can and should be predicted through the behavior of the atoms in the crystal. The nuclei are treated as point charges, and

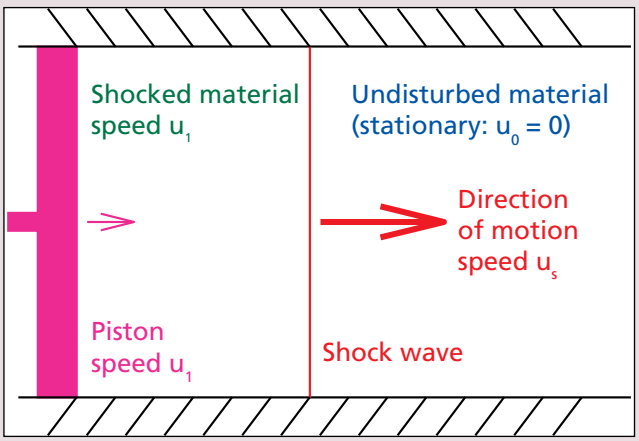

Shock compression. The shock wave transmits information about the piston to the undisturbed material ahead. Rankine-Hugoniot equations, relating the speed of the shock wave to the driving pressure, are derived by considering the conservation of mass, momentum, and energy for material passing through the shock.

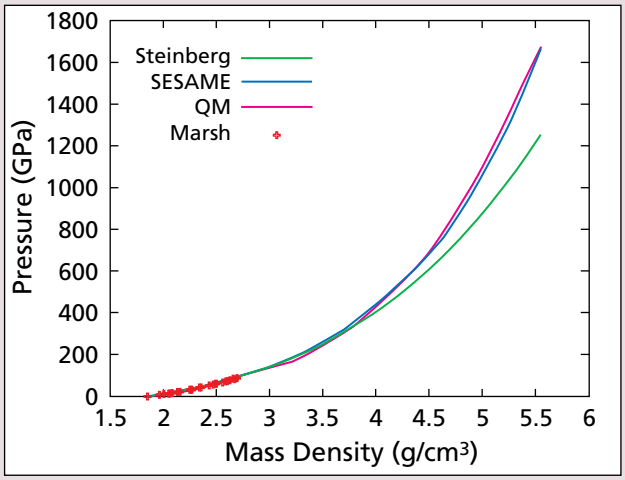

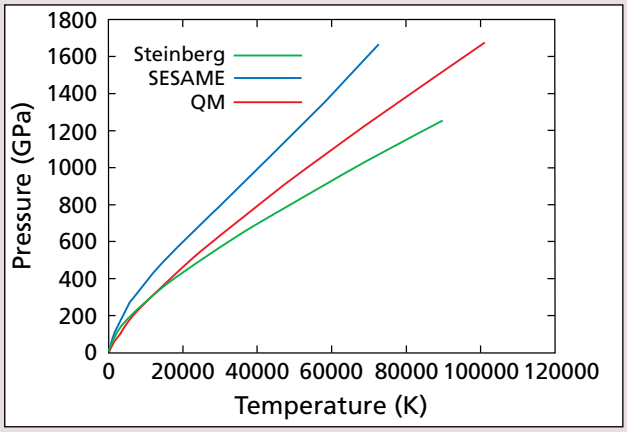

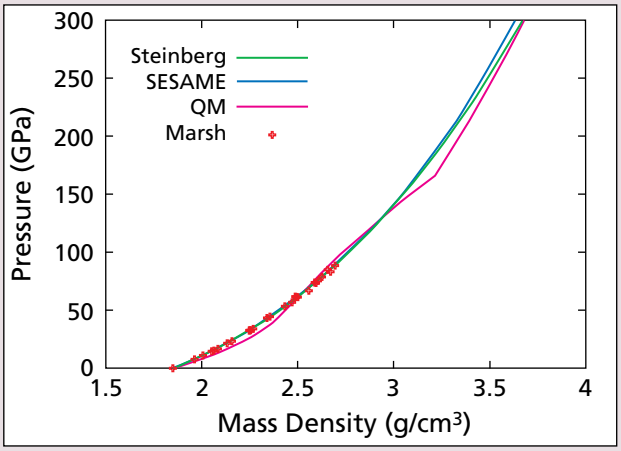

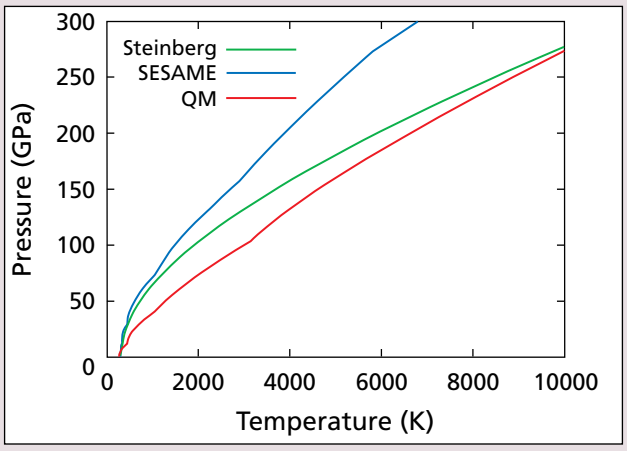

Shock Hugoniot. These graphs show the locus of shocked states that are reached from a fixed initial state by the passage of shocks of different pressure. An experiment with a single shock pressure gives a single point on the curve. The principal Hugoniot is for material that initially was at STP. Temperatures for shocked beryllium are not known accurately. These graphs show different estimates of the EOS of beryllium. Note the excellent agreement (*upper left*) with previous pressure-mass experiments, as shown in detail (*lower left*), and pressure-temperature (*upper right*) experiments, as shown in detail (*lower right*). QM is the quantum mechanical EOS; Marsh is the LANL shock compendium.

the electrons as smeared-out wave functions using quantum mechanics. This approach works well when a crystal can be represented by a reasonably small number of atoms: the EOS, the elastic constants, and phase transitions can be predicted in this way.

Tens of thousands to millions of atoms are needed to represent the defects in crystals that mediate plastic flow, so quantum mechanical simulations of this scale are not practical at present. Melting could require hundreds to millions of atoms but quantum mechanical simulations are feasible only with a few hundred atoms; to cope with more, we use molecular dynamics simulations, ignoring the electrons as physical objects and treating the atoms as points that interact through an interatomic potential (IAP). The challenge is to derive an IAP that adequately represents interaction between the atoms. The properties of beryllium are relatively difficult to represent with an IAP, and existing IAPs for beryllium are not very accurate. Although we are developing improved IAPs, we rely on experiments for plasticity and melting data.

To predict the EOS, we made quantum mechanical calculations of the electron states as a beryllium crystal was compressed and heated. We also calculated the restoring forces on atoms as they were displaced from their equilibrium positions; this information allowed us to predict the vibrational modes of the atoms as the crystal was heated. The result is a pair of tabular functions relating the pressure p and internal energy e of the crystal to its

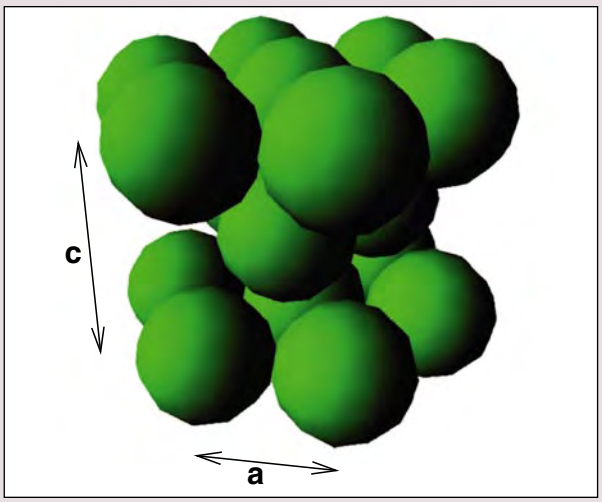

Definition of *a* and *c* axes for atoms in a hexagonal structure.

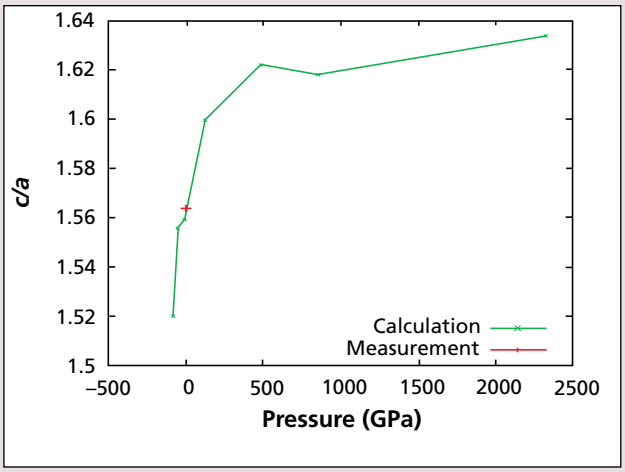

Calculated variation of *c/a* ratio with pressure, and value measured at STP.

density ρ and temperature T: $p(\rho,T)$ and $e(\rho,T)$. In this form, the EOS can be used in simulations of the time-dependent response of any material to loading and heating. Our predicted EOS agrees well with measurements of high-pressure states made using shock-wave experiments.

An advantage of this theoretical approach is that the EOS includes temperature, which is extremely difficult to measure in a shock-wave experiment. The calculations also allow us to predict how the "width" and "height" of the crystal (the c/a ratio) vary relative to each other under compression. The c/a ratio for beryllium at room temperature and 1 atm (i.e., at the standard temperature and pressure, or STP) is unusually small; our calculations reproduce this value well, giving confidence in our predictions

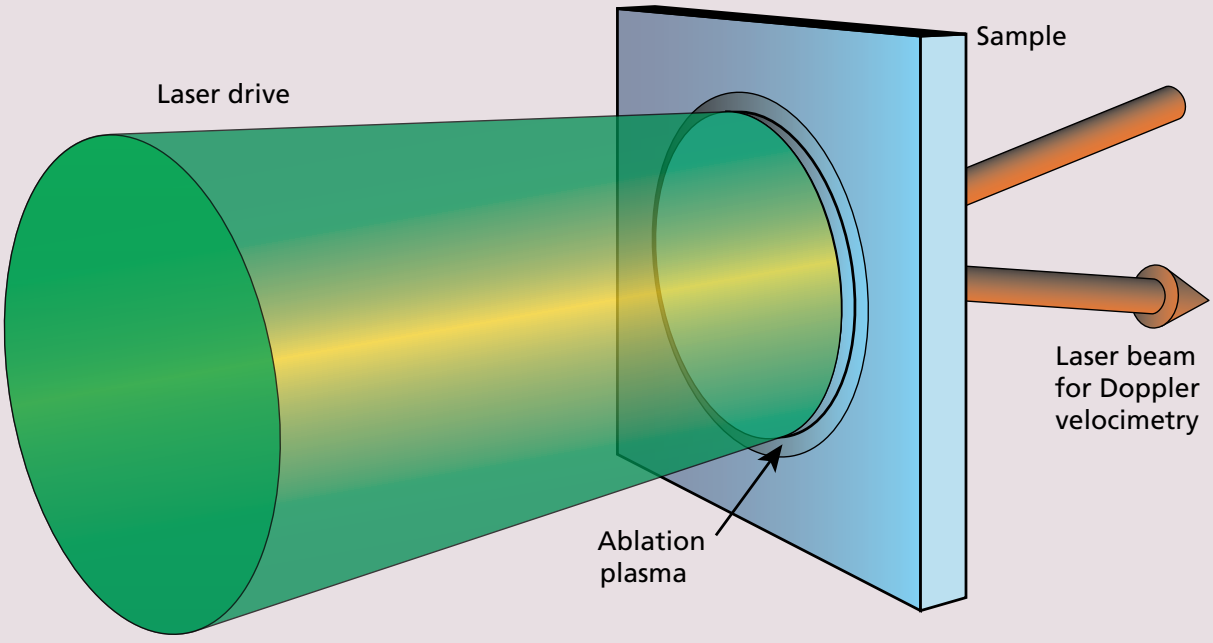

Schematic of laser ablation experiment on material response. The laser pulse creates a region of plasma, driving a shock wave into the sample. Motion of the opposite surface is monitored by Doppler velocimetry using a second laser.

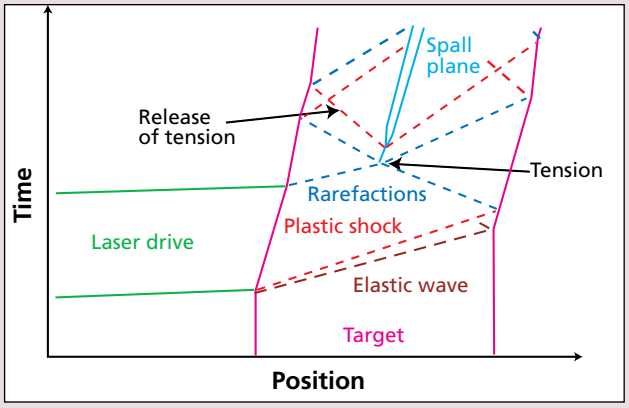

Position-time diagram of waves induced by laser ablation. Note the elastic precursor running ahead of the initial plastic shock. Information on the flow stress can be derived from the velocity history of the surface as the elastic and plastic waves appear.

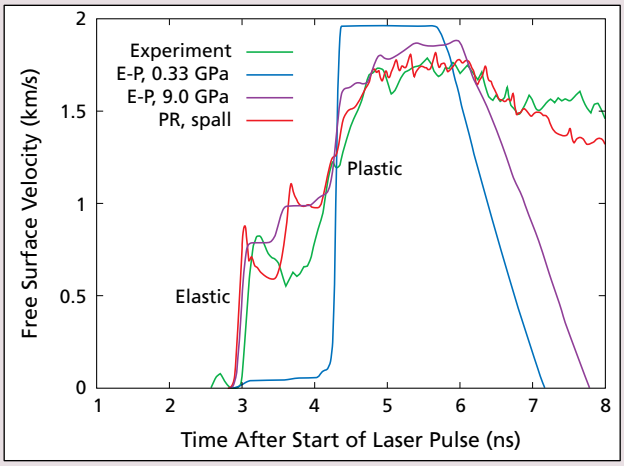

Velocity history from the free surface of a beryllium crystal, compared with simulations using different models of plasticity. Elastic-plastic (E-P) simulations are the simplest models of plasticity; 0.33 GPa is a typical flow stress on microsecond time scales. The elastic wave breaks out at the correct time, but the amplitude is too low and the shape of the plastic wave is incorrect. Increasing the flow stress to 9 GPa improves the amplitude but not the shape. The plastic relaxation (PR) model reproduces the shape of the elastic wave more accurately; this model did not include work hardening, so the rising part of the elastic wave shows stronger reverberations in the simulation than we observed experimentally. The PR simulation also included spall, improving the match after the peak of the plastic wave. Note that more accurate simulations of the elastic wave also improve the match in the plastic region.

for compressed states because the *c/a* predictions included no data for the STP state.

To predict the elastic constants, we made similar quantum mechanical calculations as the crystal was distorted (strained) by compression along different crystal directions and by shearing different pairs of faces. In each case, we used the electron states to calculate stress on the crystal; the elastic constants are the rates with which stress changes with strain. We repeated the calculations for several different compressions, giving the elastic constants as functions of compression. Again, the values we predicted for STP agreed reasonably well with the measured values, giving us confidence that our predicted variation with compression is also reasonable.

Measuring Crystal Properties

The rate of plastic flow, which is related to the elastic strain or stress that the material can support before flow occurs (also called the yield stress), depends greatly on the time available for crystal defects to move—and therefore on the thickness of the component.

We used LANL's Trident laser to induce shock waves in beryllium crystals 40- to 100-μm thick—similar to the 150-μm thickness of the ignition capsule—and studied the shape of elastic waves that run ahead of the shock. From these waves, we inferred parameters in a plasticity model that represents the properties of the defects accurately.

For a range of drive pressures, the elastic wave outruns the shock. Wave amplitude is set by yield stress and its precise shape gives more details that constrain parameters in the plasticity model. Plastic flow occurs as defects—dislocations and twin boundaries—move along planes in the lattice of atoms (the slip systems) that comprise the crystal. The average speed of a defect's movement across a plane depends on the elastic shear stress resolved over that plane; generally, several different slip systems may be active simultaneously as a crystal deforms. The stress required to activate slip systems may vary, as may the population of defects able to mediate strain in each slip system. Our studies included these variations with experiments on beryllium crystals of different orientations.

Having developed a plasticity model for single beryllium crystals, we can predict the response of a given microstructure to loading and heating. Because it is crucial to test the predictions, we will obtain elastic-

wave data from polycrystalline material with microstructures relevant to the ignition capsule. We have already measured the precursor shape and amplitude in copper-doped beryllium that was prepared by sputtering, and in rolled beryllium foils. Future experiments will measure the roughness of a shock wave after it propagates through polycrystalline material.

The melting temperature of most materials increases when the material is compressed. Shock waves passing through an object deposit heat and cause compression. At higher pressures, an increasing proportion of the energy of the shocked state is thermal; at sufficiently high shock pressures, any metal will melt. The pressure required for shock melting in beryllium has not been established, but is thought to be approximately 1.5 to 2.5 million atm and may vary with the time scale of the experiment.

We have begun studies of shock melting in beryllium using high-speed projectiles to induce high-pressure shock waves on impact with a sample. Melt can be seen after the shock has passed through some thickness of material. For example, if the sample melts, the release (deceleration) wave following the shock wave will run more slowly because it contains no contribution from elastic strain. Also, when melt occurs during compression or release, the change in volume and the disappearance of elastic stresses can lead to a change in velocity. We have observed candidate signatures for melt on release and plan to refine our measurements with further experiments. These impact experiments also measure high-pressure states, which we have found are consistent with our theoretical EOS.

Microstructural Specifications

In parallel with developing beryllium response models under dynamic loading and heating, we are developing theoretical and experimental tools to study instability seeding in ignition-capsule microstructures. These studies will allow us to define specifications for the microstructure and the high-energy preheating component of the x-ray drive so that any perturbations in the shape of the imploding capsule remain within acceptable levels.

We have performed continuum mechanics simulations of the response of a given microstructure to the loading history induced at NIF to predict stress and velocity fluctuations caused by the microstructure. We are establishing techniques to use these fluctuations in implosion simulations to predict acceptable amplitudes and therefore acceptable crystal sizes and textures in the microstructure. To date, our resolved-microstructure simulations used simplified models of the drive and beryllium plasticity. Future calculations will include a more complete plasticity model and will use a radiation hydrodynamics module that we are developing for our continuum mechanics code.

We have developed hohlraum designs for use on the University of Rochester's OMEGA laser and the first set of four beams at NIF to reproduce some aspects of the drive expected from the complete set of NIF beams. We are particularly concerned with the x-ray preheat environment, the loading history during the first few nanoseconds, and the strong acceleration phases that cause instabilities to grow. We are using these experiments—particularly at OMEGA—to verify predictions of instability seeding in samples of candidate capsule material.

Taken together, this series of experiments, theory, and simulations is the basis of our understanding of instability seeding in the microstructure of beryllium-based ignition capsules, and is a source of useful fundamental research into shock and radiation physics and the response of materials to dynamic loading. NWJ

Point of contact:
Damian C. Swift, 667-1279, dswift@lanl.gov

Other contributors to this article are James Cobble, Sheng-Nian Luo, David Montgomery, Dennis Paisley (Plasma Physics Group, Physics Division); Thomas Tierney (Hydrodynamics and X-Ray Physics Group); Barbara Devolder, Robert Goldman, Nelson Hoffman, Ian Tregillis (Plasma Physics Group, Applied Physics Division); Jason Cooley (Metallurgy Group); Arthur Nobile (Polymers and Coatings Group); Marcus Knudson (SNL); and John Lindl (LLNL).

Development of a Laser Workhorse Detonator

Concerns over the electrical hazards and safety of our experiments and firing sites are paramount in Dynamic Experimentation (DX) Division. Located in the Jemez Mountains, our firing sites frequently shut down during lightning events (New Mexico ranks second in the nation for lightning-caused deaths, injuries, and casualties).

To prevent injury in these stop-work situations, our DX engineers developed a laser workhorse detonator (LWHD), the ER-459, that eliminates an electrical path through the detonator to the explosive. Our detonator substitutes the standard electrical firing cable with a glass fiber-optic cable.

LANL historically has conducted experiments with two types of electroexplosive detonators—the exploding bridgewire (EBW) and the exploding foil initiator (EFI), sometimes called a "slapper."

LANL-designed laser detonators improve firing-site safety.

Since its invention during the Manhattan Project, the metallic EBW detonator has been the most-used high-power detonator for everything from explosive experiments to weapon systems. The EBW detonator uses electrical current from a capacitor discharge to vaporize a small, hair-thin wire. The shock and subsequent plasma that result from the bursting wire drive energy into a low-density high explosive (HE), which initiates the detonation process.

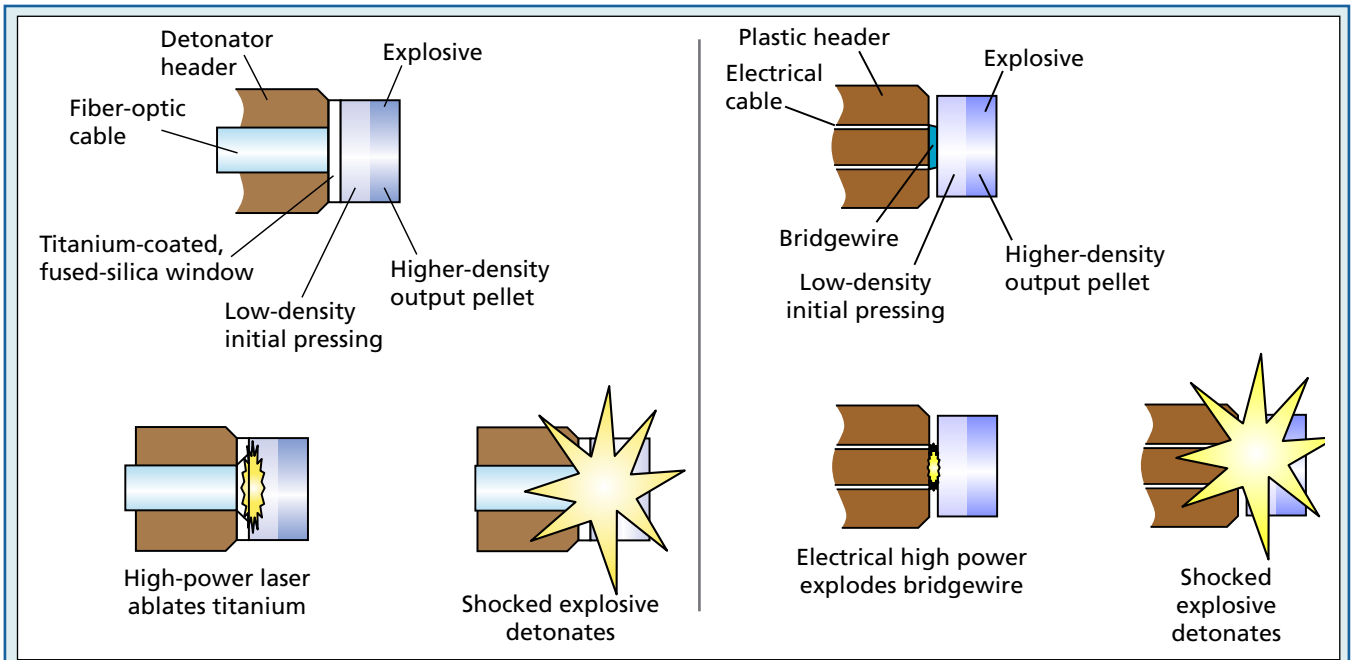

Laser and standard EBW detonation processes. In the laser EBW (*left*), energy from a high-power laser, coupled through a glass fiber-optic cable, is deposited on a thin titanium film. This energy ablates the titanium, delivering a high-pressure, high-temperature impulse to a low-density HE, which initiates detonation. The standard EBW (*right*) delivers a high-power electrical pulse through a hair-thin wire. This pulse "explodes" the wire, delivering a high-pressure, high-temperature impulse to the low-density HE, which initiates detonation.

The EFI detonator (the slapper) uses the burst from an electrically heated thin foil to propel a dielectric flying disc. This disc impacts a high-density explosive, creating a shock wave that detonates the explosive.

Both the EBW and EFI require hundreds of kilowatts of electrical power to operate reliably. However, lightning strikes and electrostatic discharge (ESD) from the human body and/or electrical equipment could provide enough stimulus to trigger these detonators.

Preventing ESD is critical to firing site safety because both EBW and EFI detonators output directly into the main explosive charge. By replacing the electrical firing cable with a glass fiber-optic cable, we have isolated the detonator from electrical hazards: with certain design features, fiber-optic cable will not propagate electrical energy.

Laser-Driven Detonator

The concept of a laser-driven detonator is not new. Since the early 1970s, scientists at LANL, LLNL, and SNL have worked to develop laser-driven analogous systems for our electrical detonators (both EBW and EFI). Most laser detonator work in the last 15 years has focused on laser-driven flyers, the optical analogy to the EFI (slapper) detonator. This type of detonator is difficult to engineer due to the very specific nature of the laser energy's spatial and temporal pulse shape that is required to propel a flat flyer and to detonate explosives predictably.

Our current research effort focuses on an LWHD (ER-459) that we call the "laser EBW" because it is almost identical in stimuli and function to the EBW: laser energy vaporizes a thin metallic film, producing both shock and plasma,

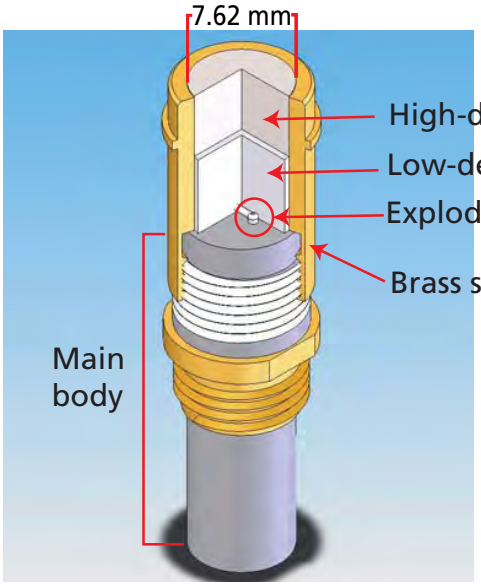

SE-1 EBW detonator. A commonly used EBW detonator, the standard brass electrical detonator (SE-1), is used in experiments to detonate large charges and light argon candles as timing markers. Because using the SE-1 during thunderstorms can be dangerous, DX researchers developed an LWHD (ER-459) that is identical in shape and explosive output to the SE-1 but offers the increased safety of a glass fiber-optic coupled laser system. Similarities in the mechanical shape and handling of the two detonators simplify replacing existing EBW hardware without major changes to the hardware or setup used in HE experiments.

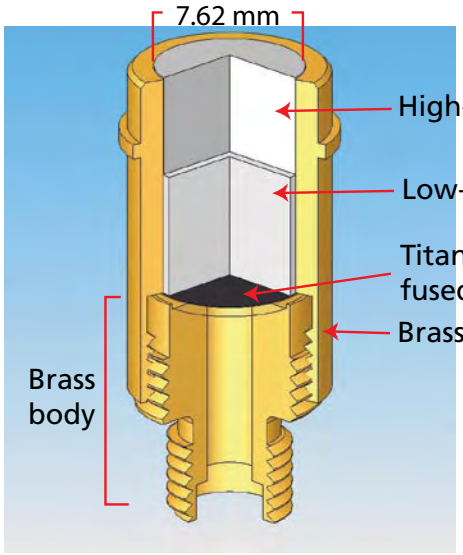

Laser EBW detonator. A nonconductive glass fiber-optic cable makes this LWHD (ER-459) safer to use during lightning events. The ER-459 uses the same sleeve and output pellet as the SE-1 detonator but replaces the plastic body with a brass body and the electrically conductive connection with the fiber-optic connector. A groove in the body holds a 0.5-mm-thick x 8-mm-diameter titanium-coated, fused-silica window between the initial pressing of the explosive PETN and the brass body. DX-1 Group inspects and assembles both the SE-1 and the ER-459 detonators using standard manufacturing processes.

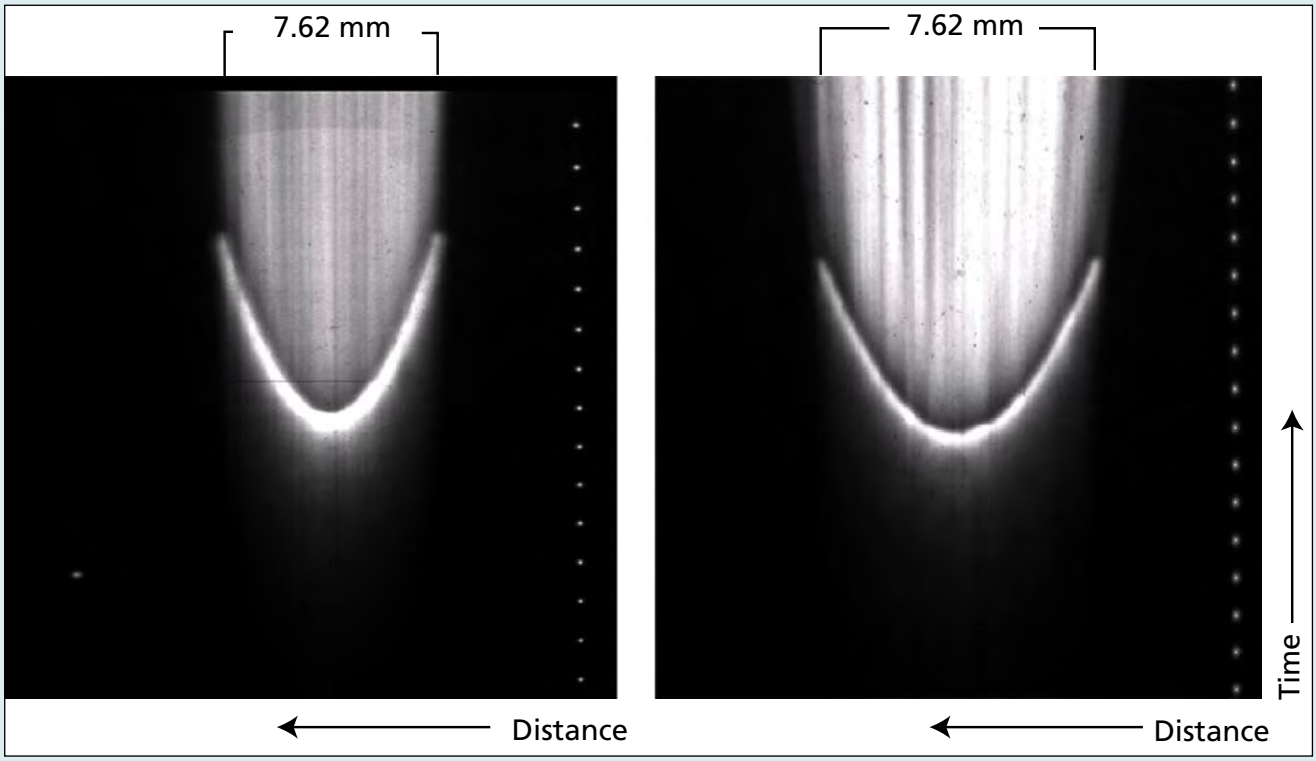

Detonation breakout. The streak record, captured with an electronic streak camera, shows the detonation breakout pattern on the detonator face. The camera records time from initiation to detonation; dots at the right edge of the photo indicate 20-ns increments. We use the detonation wave-shape output to assess similarities in SE-1 (*left*) and ER-459 (*right*) detonation characteristics. Differences in experimental setup (e.g., distance from the camera) are evident in comparisons of these streak records. Our measurement algorithm corrects for these differences.

which create a deflagration-to-detonation transition in low-density pentaerythritol tetranitrate (PETN). This transition is similar to the initiation mechanism in an electrical EBW.

The main advantage of the laser EBW (LWHD) over the laser flyer (EFI, or slapper) derives from the laser EBW's less-stringent temporal and spatial energy needs, which lessen requirements for laser output and fiber cable routing and lead to a more-robust laser detonator design.

However, the laser EBW's greatest advantage is its replacement of the conductive cable with a nonconductive fiber-optic cable. This replacement removes the detonator's susceptibility to accidental detonation from lightning or ESD.

Both EBW systems (electrical and laser) vaporize small amounts of metal to create shock waves and hot plasma that drive an explosive chemical reaction. This similarity allowed us to develop a laser-driven device with performance and detonation output characteristics that are nearly identical to those of the standard EBW detonator—making a direct, drop-in replacement possible for our numerous types of EBW detonator systems.

The laser detonator uses a high-power laser whose output pulse of a few megawatts is delivered by a 400-µm glass fiber-optic cable through a 0.5-mm glass window onto a thin film of titanium. The resulting power density of approximately 2 GW/cm^2 vaporizes the 2,500-Å (0.25-µm)-thick titanium film. The shock and plasma from the exploding film drive into a low-density pressing of PETN, causing buildup to detonation approximately 1 mm from the film surface. The PETN charge transfers to a high-density explosive output pellet. Although PETN detonation can occur without the titanium film, we found that using the film significantly lowers the minimum energy required for detonation.

Function time, the time from initiation through buildup to detonation and the subsequent run of the detonation wave to the end of the detonator, is

the most important characteristic of a detonator. Most of the function time can be accounted for by considering the speed of the detonation wave propagating through the explosive. We have measured an excess function time, the time not accounted for, of 100 to 200 ns in the laser detonator, which is comparable to an EBW detonator buildup to detonation. Thus our work demonstrates that initiation in an EBW detonator is a deflagration-to-detonation process. In this process, deflagration produces a compression wave that moves outward into the low-density HE powder in a more gradual compression wave rather than the usual large-gradient shock wave. A characteristic of this type of ramp wave is that it produces less heat and/or chemical reaction than a shock wave. Our experiments have documented this ramp-wave buildup to detonation in an EBW and similar ramp-like waves in laser detonators. Thus we conclude that the initiation mechanisms for the laser and EBW detonators are similar.

The Detonator Technology (DX-1) Group developed a computer algorithm to characterize the detonation properties of each detonator we fired. This program measures two qualities of detonation: function time and apparent center of initiation (COI). The function time portion of the program incorporates the time from the start of either electrical current or laser pulse, which we measure with an oscilloscope, and wave breakout, which we measure in the streak record that is recorded by an electronic streak camera. The streak record is an optical recording of light output from a detonator. We computed the apparent COI by extracting the observed wave breakout profile and determined the apparent point of origin of the Huygens-like spherical detonation wave. This COI calculation corrects for dissimilarities in experimental setups. The COI quantitatively measures the wave shape of the detonation breakout. These two measurement techniques allow us to compare the wave characteristics of two different detonators such as the EBW and the LWHD.

Accomplishments

We have manufactured and tested three lots of LWHDs using the same titanium film and manufacturing processes for each lot. Our results show consistency in both function time and COI across all three lots.

Working with our partners at Kansas City Plant, we have developed a rack-mounted firing unit to house the LWHD laser fireset (firing system) and its electronics. This system incorporates the laser and triggering devices that can enhance safety at LANL firing sites.

In addition to the standard brass LWHD, we also designed and fabricated an all-plastic laser detonator whose parts are invisible to both x-rays and proton radiography. In an experiment, the metallic detonator housing (particularly the copper detonator cable) obscures parts of the x-ray image. The all-plastic housing and fused-silica, fiber-optic firing cable are invisible to x-rays, giving an unprecedented view of the explosive area around the detonator and detonator cable.

In conclusion, we have designed and fabricated a fieldable workhorse detonator and firing system that eliminate several major experiment-related safety concerns. Similarities in LWHD and existing EBW initiation mechanisms simplify part replacement. We also have demonstrated our ability to fabricate these detonators with repeatable performance and our ability to adapt our basic concept to evolving experimental requirements.

We believe this system is ready for use at our firing sites. NWJ

Points of contact:
Adrian Akinci, 606-0394, akinci@lanl.gov
Keith Thomas, 665-5248, thomask@lanl.gov

Other contributors to this project are Alan Munger, Lawrence Nunn, Steven Clarke, Michael Johnson, David Montoya, Sylvia Trujillo, the Detonator Fabrication Team, Michael Martinez, Dennis Jaramillo, Sherri Bingert, and Phil Howe.

ATOMICS: Working Safely at NMT

Workers at Nuclear Materials Technology (NMT) Division take safety personally.

Incorporating the process known as Allowing Timely Observations Measures Increased Commitment to Safety (ATOMICS) into individual work practices, each member of the division accepts responsibility for personal work behaviors; the result is a marked improvement in safety throughout the division.

Introduced at NMT in January 2000, ATOMICS is an interactive, behavior-based safety process that

- measures and manages safety-related behaviors to reduce the frequency and severity of accidents,
- promotes personal involvement in the process on a regular basis, and
- uses two-way feedback between workers to encourage and reinforce desired safe behaviors.

Based on personal initiative, ATOMICS places responsibility for workplace safety on each member of the work force. At all organizational levels, individuals accept responsibility for their safety and that of others.

An ATOMICS steering team trains workers in a peer-to-peer observation process that tracks both safe and at-risk behaviors to enhance safety awareness and prevent on-the-job injuries and accidents. Composed of technicians and administrative staff, the steering team collects observational data from individual workers to identify trends in at-risk behaviors. The team presents these data to division managers for their review once each month. These monthly data identify improvement target areas for workers, based on observed levels of exposure to unsafe conditions. Subsequent action plans from the steering team address the respective processes, procedures, and values necessary to improve workplace safety.

Prospective peer observers receive 2 days of training. Observations, which typically take no more than 15 minutes, follow an anonymous, standardized process. All suggestions for improved safety behaviors follow a no-name, no-blame rule as they flow both up and down the organizational hierarchy. Its minimal disruption to workload, anonymity, and reinforcement of improved safety awareness all contribute to ATOMICS' long-term sustainability.

Effective safety processes are based on consistent worker participation and positive feedback.

NMT's commitment to ATOMICS demonstrates the first guiding principle of LANL's Integrated Safety Management Program: management commitment and worker involvement. To further strengthen NMT's safety envelope, NMT also integrates elements of two other training concepts into division work activities. Human performance focuses on reinforcing safe behavior during all phases of work rather than on avoiding certain work habits (see "Human Performance and Highly Reliable Organizations," Issue 1, 2005, p. 30). STOP® for Managers is safety-awareness training. These concepts differ in theory and practice but both endorse the same end result—worker safety. They also promote one of NMT's core values: people are our most important resource. NWJ

Points of contact:
Jim Kleinsteuber, 667-0361, jimfk@lanl.gov
Maryrose Montalvo, 667-4988, mmontalvo@lanl.gov

Other contributors to this article are Crestina Vigil of the NMT Division Office and Dixon Wolf of the Nuclear Materials Information Management Group.

Two-way feedback (*left*) between workers identifies potentially harmful or dangerous work practices. Participants in the ATOMICS process at NMT Division accept personal responsibility for workplace safety behavior and encourage improved safety awareness throughout the division.

A peer observer (*below left*) watches as a coworker begins glovebox operations. A steering team uses the observer's findings to prepare an action plan that suggests corrective actions, if necessary.

Following a standardized process that protects the anonymity of the workers, an ATOMICS-trained NMT employee (*below right*) observes the safety behavior of a forklift operator. All findings are incorporated into a database that NMT management reviews monthly to detect trends in at-risk behaviors.

Point of View, continued from page 1

an integrated project plan, a life-cycle cost assessment, and a clear explanation of how the proposed design would revamp the present weapons infrastructure to meet transitioning national security needs.

SSP with RRW

Although our nuclear stockpile is safe and secure, incorporating RRW into stockpile stewardship will ensure the future flexibility, safety, and security of the stockpile, with the additional benefit of reducing overall life-cycle costs.

The current stockpile is costly to maintain because it uses hazardous, environmentally unfriendly materials that are expensive to remanufacture, even in the best-managed LEPs. Our legacy warheads were not designed for longevity; although we expected they would be replaced before aging issues could be important, weapons designed in the 1970s and 1980s (when nuclear testing was a viable tool) now will be kept in the stockpile into the 2040s.

The RRW feasibility study will lead to a design that is more robust and that has increased performance margins—an important issue for certification without new nuclear testing—and that is safer, more secure, and less expensive overall to manufacture. These improvements potentially could reduce life-cycle costs.

In addition, the legacy stockpile was designed before 9/11. That attack heightened our realization that we must be prepared to prevent terrorist activity here in the United States. Increasingly, the primary issue now is not simply how to maintain the current stockpile but whether we have a stockpile that meets immediate as well as future national security requirements.

The timeline for producing an RRW (2012 to 2015) is an opportunity to exercise the Nuclear Weapons Complex (NWC) to renovate current nuclear weapons systems, achieving reliable weapons elements that can be manufactured and certified without nuclear testing. In turn, RRW production would drive changes in the NWC, making it a more-efficient, more-responsive entity.

Other Drivers

The 2001 Nuclear Posture Review established the need to transition to a New Triad—a new architecture for most national security missions—that includes nonnuclear and nuclear strike capabilities and defenses and a responsive infrastructure. Because the US may someday be required to design and produce new warheads to meet presently unforeseen threats or to rebuild existing warheads to correct potential problems as they are identified, a responsive infrastructure—that also could lead to overall stockpile reduction—is a key component of the future NWC.

The initiation of an RRW program is also driven by the pending loss of nuclear warhead design expertise.

The United States has not developed and fielded a new warhead in more than 10 years; many scientists and engineers who designed and tested our current stockpile systems are approaching retirement age. Because future threats to national security could require new or different nuclear weapons capability, we must maintain the ability to produce nuclear warheads. A new generation of designers must be trained before we lose the expertise of the designers who have actual nuclear testing experience.

The successful RRW will replace expensive, aging warheads with a smaller stockpile that is safe and secure, that reduces the need for testing, and that ensures a more-responsive nuclear infrastructure. Ultimately, a successful RRW must demonstrate cost savings over the total life cycle of the warhead while stimulating transformation of the infrastructure to one that is more cost-effective and responsive.

Most importantly, the RRW must provide the same or better confidence in certification without nuclear testing that we have demonstrated for the past 10 years through stockpile stewardship. NWJ

A BACKWARD GLANCE

Eyewitnesses to Trinity

July 16, 2005, marked the 60th anniversary of the world's first nuclear explosion. Conducted at the Trinity Test Site near Alamogordo, New Mexico, the test was needed to determine if a radical new weapon, nicknamed "the gadget," would work. Its designers were confident that their calculations were correct although they could not pinpoint how large or powerful the detonation would be.

At base camp 10 miles from ground zero, Enrico Fermi protected his face "by a large board in which a piece of dark welding glass had been inserted." His first impression of the explosion was "the very intense flash of light" that seemed "brighter . . . than in full daylight." Through the glass, he saw "a conglomeration of flames that promptly started rising," becoming "a huge pillar of smoke with an expanded head like a gigantic mushroom that rose rapidly beyond the clouds." About 40 seconds after the explosion, the air blast reached him. He estimated its strength by "dropping from about six feet small pieces of paper before, during and after the passage of the blast wave," concluding that it corresponded "to the blast that would be produced by ten thousand tons of T.N.T. [*sic*]" The actual yield was about 21 kt.

Victor Weisskopf, also at base camp "on a little ridge about 100 yds. [*sic*] east of the water tower," watched indirectly "through the dark glass" so he could see the deflected light. "When the explosion went off," he wrote, "I was first dazzled by this indirect light which was much stronger than I anticipated, and I was not able to concentrate upon the view through the dark glass." Looking directly at the explosion 3 seconds later, he saw "a reddish glowing smoke ball rising with a thick stem of dark brown color . . . surrounded by a blue glow." The shock wave through the clouds was "plainly visible as an expanding circle all over the sky where it was covered by clouds." Weisskopf "felt very strongly the heat radiation all over the exposed parts of my body." The sound wave arrived "after about 45 seconds and it struck me as being much weaker than anticipated," he wrote.

About 20 miles from the detonation point, Captain R. A. Larkin, seated on the ground, deliberately had his "eyes fixed on the ground immediately in front . . . to avoid the blinding flash" he expected. "My first impression," he said, "was of a sudden brilliant lighting of the surrounding landscape, accompanied by a momentary flash of heat." He was surprised that the illumination, "initially quite brilliant, continued to increase for a brief interval." His dark glass filter was "designed to eliminate over 99% of the light." But when he looked through it, he was momentarily blinded, much as he would have been by a "close flash of lightning on a dark night." He noted a "ball of light" and below it "a column of red flame about 150 or 200 yards in diameter. Flickering red reflections were distinctly seen on the clouds above the ball of light."

"At about ten seconds after detonation . . . the ball and column took on the shape of a vast mushroom." Ten minutes after detonation the cloud was still "quite distinct and rising rapidly." Fifteen minutes later, the pillar under the cloud had faded, and after 30 minutes the cloud "faded from view."

At Military Police Post No. 2 (20 miles from "zero point"), Ralph Carlisle Smith "stretched out on a blanket facing south" and looked through a welder's glass with his left eye. The flash temporarily blinded his open, unprotected right eye but through his left he saw the "amazingly bright" light that "turned yellow, then red, and then beautiful purple," eventually rising "in something of a toadstool effect." After the cloud turned to a "ponderously" moving cylinder of white smoke and a "hole was punched well above the white smoke column," he saw "two fog rings . . . well above the white smoke column." Then, he said, "There was a spontaneous cheer of the observers." Although he did not report heat, Smith noted that roughly 1.5 minutes after the light "a sharp loud crack swept over us—it reverberated through the mountain[s] like thunder." He estimated the fireball was "1 to 2 miles wide." A nearby observer guessed the strength to be "at least 5000 tons and probably a lot more." NWJ

For these and the accounts of other observers in the Trinity test area, see the Laboratory's history page at *http://www.lanl.gov/history/atomicbomb/trinity.shtml*.